Published OnlineFirst February 26, 2013; DOI: 10.1158/1541-7786.MCR-12-0428

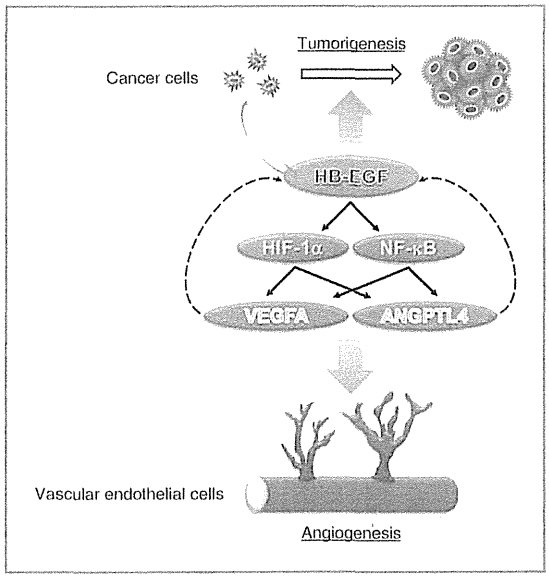

Figure 6. Molecular regulation of tumorigenesis and angiogenesis is centered on HB-EGF in TNBC. HB-EGF is an essential molecule for 3D cell growth involved in tumorigenesis. During tumorigenesis, the growth of blood vessels is essential to support the indefinite proliferation of cancer cells. We show that upregulation of HB-EGF expression accompanying tumorigenesis enhances the expression of VEGFA and ANGPTL4. This occurs via activation of HIF-1α and NF-κB, mediated by ERK and AKT signaling pathways (solid arrows), resulting in aberrant angiogenesis. Inhibition of VEGFA or ANGPTL4 expression enhanced the HB-EGF expression (dotted arrows). Therefore, HB-EGF may represent a rational target molecule for TNBC therapy.

the mitogenic activity of HB-EGF through inhibition of EGFR binding and inhibits the ectodomain shedding of HB-EGF or protein synthesis by binding to uncleaved form of HB-EGF (44). We have also developed a novel anti-HB-EGF chimeric antibody, cKM3566, which has 2 antitumor mechanisms. This antibody is capable of neutralizing the soluble form of HB-EGF and also induces antibody-dependent cellular cytotoxicity, exhibiting potent *in vivo* antitumor activity (45). Recently, we have completed a phase I study for the use of CRM197 in patients with recurrent ovarian cancer in Fukuoka University Hospital (Fukuoka, Japan) under the approval of the institutional Ethical Committee. While encouraging, the translation of these interesting preclinical/early clinical findings into clinical use of HB-EGF inhibitors is still a work in progress. We conducted gene expression analysis using BT474 and MCF7-HER2 as representative HER2-amplified breast cancer cell lines. Similar to the enhanced expression of HB-EGF, expression of VEGFA and ANGPTL4 were also significantly augmented in 3DC and in tumor xenografts in BT474 and MCF7-HER2 cells, compared with 2DC (data not shown). Although further analysis in breast cancer tissues is required, it is plausible that elevated VEGFA or ANGPTL4 contributes to tumor development in specific subtypes of breast cancer.

Disclosure of Potential Conflicts of Interest

No potential conflicts of interest were disclosed.

Authors' Contributions

Conception and design: F. Yotsumoto, S. Miyamoto
Development of methodology: M. Kuroki, S. Miyamoto
Acquisition of data (provided animals, acquired and managed patients, provided facilities, etc.): F. Yotsumoto, E. Tokunaga, H. Yamada, K. Nakajima, S.O. Nam, K. Miyata, M. Koyanagi, K. Doi
Analysis and interpretation of data (e.g., statistical analysis, biostatistics, computational analysis): F. Yotsumoto, E. Tokunaga, H. Yamada, K. Nakajima, S.O. Nam, K. Miyata, M. Koyanagi, K. Doi
Writing, review, and/or revision of the manuscript: F. Yotsumoto, S. Miyamoto
Administrative, technical, or material support (i.e., reporting or organizing data, constructing databases): F. Yotsumoto, E. Tokunaga, E. Oki, Y. Maehara, S. Shirasawa, M. Kuroki, S. Miyamoto
Study supervision: Y. Maehara, S. Shirasawa, M. Kuroki, S. Miyamoto

Acknowledgments

The authors thank Akina Narimatsu and Takako Koshimizu for technical assistance.

Grant Support

This work was supported in part by a Grant-in-Aids for Young Scientists (B) (no. 22790536), Scientific Research (C) (no. 23592470), and the Center for Advanced Molecular Medicine, Fukuoka University from the Ministry of Education, Culture, Sports, Science and Technology (Tokyo, Japan), a Grant-in-Aid from the Kakihara Science and Technology Foundation (Fukuoka, Japan) to S. Miyamoto and a Grant-in-Aid from Kyowa Hakko Kirin Co. Ltd. (Tokyo, Japan) to S. Miyamoto.

The costs of publication of this article were defrayed in part by the payment of page charges. This article must therefore be hereby marked *advertisement* in accordance with 18 U.S.C. Section 1734 solely to indicate this fact.

Received July 9, 2012; revised January 22, 2013; accepted February 6, 2013; published OnlineFirst February 26, 2013.

References

1. Bergers G, Benjamin LE. Tumorigenesis and the angiogenic switch. Nat Rev Cancer 2003;3:401–10.
2. Carmeliet P, Jain RK. Molecular mechanisms and clinical applications of angiogenesis. Nature 2011;473:298–307.
3. Potente M, Gerhardt H, Carmeliet P. Basic and therapeutic aspects of angiogenesis. Cell 2011;146:873–87.
4. Folkman J. Angiogenesis in cancer therapy—endostatin and its mechanisms of action. Exp Cell Res 2006;312:594–607.
5. Persano L, Crescenzi M, Indraccolo S. Anti-angiogenic gene therapy of cancer: current status and future prospects. Mol Aspects Med 2007;28:87–114.
6. Chan DA, Giaccia AJ. PHD2 in tumour angiogenesis. Br J Cancer 2010;103:1–5.
7. Hanahan D, Folkman J. Patterns and emerging mechanisms of the angiogenic switch during tumorigenesis. Cell 1996;86:353–64.
8. Miles DW. Recent advances in systemic therapy. When HER2 is not the target: advances in the treatment of HER2-negative metastatic breast cancer. Breast Cancer Res 2009;11:208.
9. Di Cosimo S, Baselga J. Management of breast cancer with targeted agents: importance of heterogeneity. Nat Rev Clin Oncol 2010;7:139–47.
10. Nalwoga H, Arnes JB, Stefansson IM, Wabinga H, Foulkes WD, Akslen LA. Vascular proliferation is increased in basal-like breast cancer. Breast Cancer Res Treat 2011;130:1063–71.

Published OnlineFirst February 26, 2013; DOI: 10.1158/1541-7786.MCR-12-0428

11. Miller K, Wang M, Gralow J, Dickler M, Cobleigh M, Perez EA, et al. Paclitaxel plus bevacizumab versus paclitaxel alone for metastatic breast cancer. N Engl J Med 2007;357:2666–76.
12. Brufsky AM, Hurvitz S, Perez E, Swamy R, Valero V, O'Neill V, et al. RIBBON-2: a randomized, double-blind, placebo-controlled, phase III trial evaluating the efficacy and safety of bevacizumab in combination with chemotherapy for second-line treatment of human epidermal growth factor receptor 2-negative metastatic breast cancer. J Clin Oncol 2011;29:4286–93.
13. Jain RK, Duda DG, Clark JW, Loeffler JS. Lessons from phase III clinical trials on anti-VEGF therapy for cancer. Nat Clin Pract Oncol 2006;3: 24–40.
14. Riese DJ, Stern DF. Specificity within the EGF family/ErbB receptor family signaling network. Bioessays 1998;20:41–8.
15. Higashiyama S, Abraham JA, Miller J, Fiddes JC, Klagsbrun M. A heparin-binding growth factor secreted by macrophage-like cells that is related to EGF. Science 1991;251:936–9.
16. Miyamoto S, Hirata M, Yamazaki A, Kageyama T, Hasuwa H, Mizushima H, et al. Heparin-binding EGF-like growth factor is a promising target for ovarian cancer therapy. Cancer Res 2004;64:5720–7.
17. Yotsumoto F, Yagi H, Suzuki SO, Oki E, Tsujioka H, Hachisuga T, et al. Validation of HB-EGF and amphiregulin as targets for human cancer therapy. Biochem Biophys Res Commun 2008;365:555–61.
18. Yotsumoto F, Oki E, Tokunaga E, Maehara Y, Kuroki M, Miyamoto S. HB-EGF orchestrates the complex signals involved in triple-negative and trastuzumab-resistant breast cancer. Int J Cancer 2010;127: 2707–17.
19. Wang F, Liu R, Lee SW, Sloss CM, Couget J, Cusack JC. Heparin-binding EGF-like growth factor is an early response gene to chemotherapy and contributes to chemotherapy resistance. Oncogene 2007;26:2006–16.
20. Cheng CY, Kuo CT, Lin CC, Hsieh HL, Yang CM. IL-1beta induces expression of matrix metalloproteinase-9 and cell migration via a c-Src-dependent, growth factor receptor transactivation in A549 cells. Br J Pharmacol 2010;160:1595–610.
21. Ongusaha PP, Kwak JC, Zwible AJ, Macip S, Higashiyama S, Taniguchi N, et al. HB-EGF is a potent inducer of tumor growth and angiogenesis. Cancer Res 2004;64:5283–90.
22. Mizushima H, Wang X, Miyamoto S, Mekada E. Integrin signal masks growth-promotion activity of HB-EGF in monolayer cell cultures. J Cell Sci 2009;122:4277–86.
23. Murata T, Mizushima H, Chinen I, Moribe H, Yagi S, Hoffman RM, et al. HB-EGF and PDGF mediate reciprocal interactions of carcinoma cells with cancer-associated fibroblasts to support progression of uterine cervical cancers. Cancer Res 2011;71:6633–42.
24. Nakai K, Yoneda K, Moriue T, Igarashi J, Kosaka H, Kubota Y. HB-EGF-induced VEGF production and eNOS activation depend on both PI3 kinase and MAP kinase in HaCaT cells. J Dermatol Sci 2009;55:170–8.
25. Koyanagi M, Nakabayashi K, Fujimoto T, Gu N, Baba I, Takashima Y, et al. ZFAT expression in B and T lymphocytes and identification of ZFAT-regulated genes. Genomics 2008;91:451–7.
26. Semenza GL. Targeting HIF-1 for cancer therapy. Nat Rev Cancer 2003;3:721–32.
27. Aggarwal BB. Nuclear factor-kappaB: the enemy within. Cancer Cell 2004;6:203–8.
28. Tan MJ, Teo Z, Sng MK, Zhu P, Tan NS. Emerging roles of angiopoietin-like 4 in human cancer. Mol Cancer Res 2012;10:677–88.
29. Le Jan S, Amy C, Cazes A, Monnot C, Lamandé N, Favier J, et al. Angiopoietin-like 4 is a proangiogenic factor produced during ischemia and in conventional renal cell carcinoma. Am J Pathol 2003;162: 1521–8.
30. Hermann LM, Pinkerton M, Jennings K, Yang L, Grom A, Sowders D, et al. Angiopoietin-like-4 is a potential angiogenic mediator in arthritis. Clin Immunol 2005;115:93–101.
31. Ito Y, Oike Y, Yasunaga K, Hamada K, Miyata K, Matsumoto S, et al. Inhibition of angiogenesis and vascular leakiness by angiopoietin-related protein 4. Cancer Res 2003;63:6651–7.
32. Cazes A, Galaup A, Chomel C, Bignon M, Bréchot N, Le Jan S, et al. Extracellular matrix-bound angiopoietin-like 4 inhibits endothelial cell adhesion, migration, and sprouting and alters actin cytoskeleton. Circ Res 2006;99:1207–15.
33. Chomel C, Cazes A, Faye C, Bignon M, Gomez E, Ardidie-Robouant C, et al. Interaction of the coiled-coil domain with glycosaminoglycans protects angiopoietin-like 4 from proteolysis and regulates its anti-angiogenic activity. FASEB J 2009;23:940–9.
34. Dreymueller D, Pruessmeyer J, Groth E, Ludwig A. The role of ADAM-mediated shedding in vascular biology. Eur J Cell Biol 2012; 91:472–85.
35. Miyamoto S, Yagi H, Yotsumoto F, Kawarabayashi T, Mekada E. Heparin-binding epidermal growth factor-like growth factor as a novel targeting molecule for cancer therapy. Cancer Sci 2006; 97:341–7.
36. Mullenbrock S, Shah J, Cooper GM. Global expression analysis identified a preferentially nerve growth factor-induced transcriptional program regulated by sustained mitogen-activated protein kinase/extracellular signal–regulated kinase (ERK) and AP-1 protein activation during PC12 cell differentiation. J Biol Chem 2011;286:45131–45.
37. Huang YL, Shi GY, Lee H, Jiang MJ, Huang BM, Wu HL, et al. Thrombin induces nestin expression via the transactivation of EGFR signalings in rat vascular smooth muscle cells. Cell Signal 2009; 21:954–68.
38. Mancuso MR, Davis R, Norberg SM, O'Brien S, Sennino B, Nakahara T, et al. Rapid vascular regrowth in tumors after reversal of VEGF inhibition. J Clin Invest 2006;116:2610–21.
39. Batchelor TT, Sorensen AG, di Tomaso E, Zhang WT, Duda DG, Cohen KS, et al. AZD2171, a pan-VEGF receptor tyrosine kinase inhibitor, normalizes tumor vasculature and alleviates edema in glioblastoma patients. Cancer Cell 2007;11:83–95.
40. Ebos JM, Lee CR, Cruz-Munoz W, Bjarnason GA, Christensen JG, Kerbel RS. Accelerated metastasis after short-term treatment with a potent inhibitor of tumor angiogenesis. Cancer Cell 2009;15:232–9.
41. Pàez-Ribes M, Allen E, Hudock J, Takeda T, Okuyama H, Viñals F, et al. Antiangiogenic therapy elicits malignant progression of tumors to increased local invasion and distant metastasis. Cancer Cell 2009; 15:220–31.
42. Allegra CJ, Yothers G, O'Connell MJ, Sharif S, Petrelli NJ, Colangelo LH, et al. Phase III trial assessing bevacizumab in stages II and III carcinoma of the colon: results of NSABP protocol C-08. J Clin Oncol 2011;29:11–6.
43. Mitamura T, Higashiyama S, Taniguchi N, Klagsbrun M, Mekada E. Diphtheria toxin binds to the epidermal growth factor (EGF)-like domain of human heparin binding EGF-like growth factor/diphtheria toxin receptor and inhibits specifically its mitogenic activity. J Biol Chem 1995;270:1015–9.
44. Hamaoka M, Chinen I, Murata T, Takashima S, Iwamoto R, Mekada E. Anti-human HB-EGF monoclonal antibodies inhibiting ectodomain shedding of HB-EGF and diphtheria toxin binding. J Biochem 2010;148:55–69.
45. Miyamoto S, Iwamoto R, Furuya A, Takahashi K, Sasaki Y, Ando H, et al.. A novel anti-human HB-EGF monoclonal antibody with multiple antitumor mechanisms against ovarian cancer cells. Clin Cancer Res 2011;17:6733–41.

SCIENTIFIC REPORTS

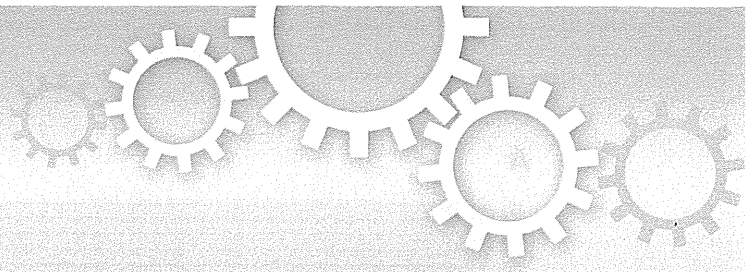

OPEN

SUBJECT AREAS:
DEVELOPMENT
TAL EFFECTOR NUCLEASE

Received
14 August 2013

Accepted
16 October 2013

Published
5 November 2013

Production of *Sry* knockout mouse using TALEN via oocyte injection

Tomoko Kato[1]*, Kohei Miyata[1,2]*, Miku Sonobe[3], Satoshi Yamashita[1], Moe Tamano[1], Kento Miura[4], Yoshiakira Kanai[4], Shingo Miyamoto[2], Tetsushi Sakuma[5], Takashi Yamamoto[5], Masafumi Inui[1], Takefumi Kikusui[3], Hiroshi Asahara[1,6,7] & Shuji Takada[1]

[1]Department of Systems BioMedicine, National Research Institute for Child Health and Development, Tokyo 157-8535, Japan, [2]Department of Obstetrics and Gynecology, Faculty of Medicine, Fukuoka University, Fukuoka 814-0180, Japan, [3]Department of Animal Science and Biotechnology, Azabu University, Kanagawa 252-5201, Japan, [4]Department of Veterinary Anatomy, The University of Tokyo, Tokyo 113-8657, Japan, [5]Department of Mathematical and Life Sciences, Graduate School of Science, Hiroshima University, Hiroshima 739-8526, Japan, [6]Department of Systems BioMedicine, Graduate School of Medical and Dental Sciences, Tokyo Medical and Dental University, Tokyo 113-8510, Japan, [7]CREST, Japan Science and Technology Agency (JST), Saitama 332-0011, Japan.

Correspondence and requests for materials should be addressed to H.A. (asahara.syst@tmd.ac.jp) or S.T. (takada-s@ncchd.go.jp)

* These authors contributed equally to this work.

Recently developed transcription activator-like effector nuclease (TALEN) technology has enabled the creation of knockout mice, even for genes on the Y chromosome. In this study, we generated a knockout mouse for *Sry*, a sex-determining gene on the Y chromosome, using microinjection of TALEN RNA into pronuclear stage oocytes. As expected, the knockout mouse had female external and internal genitalia, a female level of blood testosterone and a female sexually dimorphic nucleus in the brain. The knockout mouse exhibited an estrous cycle and performed copulatory behavior as females, although it was infertile or had reduced fertility. A histological analysis showed that the ovary of the knockout mouse displayed a reduced number of oocytes and luteinized unruptured follicles, implying that a reduced number of ovulated oocytes is a possible reason for infertility and/or reduced fertility in the KO mouse.

In most mammalian species, sex is determined by the presence or absence of the Y chromosome. In mice, the *Sry* gene locates to the minimum sex-determining region of the murine Y chromosome[1], is expressed in the male genital ridge at the time of sex determination[2] and has been proven to be a sex-determining gene based on gain-of-function experiments, i.e., the overexpression of *Sry* in XX mice achieved with transgenic mouse technology reveals a male phenotype[3]. Also in humans, the *SRY* gene has been shown to play a pivotal role in sex determination: point mutations or deletions of the *SRY* gene are found in approximately 15% of XY females, and translocated *SRY* is found in the autosomes of most XX males[4]. Although there are a number of suggestive observations, it is important to confirm the function of *Sry in vivo* using loss-of-function analyses with targeted mutagenesis in order to examine whether *Sry* is the one and only sex-determining gene on the Y chromosome and to finally confirm the *Sry* gene as the sex-determining gene and provide an animal model of XY female syndrome. However, it is difficult to create knockout (KO) mice of Y-linked genes using conventional homologous recombination-based methods with embryonic stem (ES) cells, as the process requires an adequate length of specific sequences of homologous arms to construct a KO vector, and the Y chromosome is rich in repeats.

In 2013, Sung *et al.*[5] first reported that KO mice can be produced using transcription activator-like effector nuclease (TALEN) technology without conventional homologous recombination-based methods. TALEN protein is an artificial sequence-specific endonuclease that contains *Xanthomonas* transcription activator-like effector (TALE) and a nuclease domain of FokI restriction endonuclease[6]. DNA binding domain of TALE consists of a tandem repeat of 33–35 amino acid motifs in which there are two critical adjacent amino acid pairs called a repeat variable diresidue (RVD) that determines the binding specificity for single nucleotide. There is a one-to-one relationship between the RVD and its recognition nucleotide[7,8]. Using this code, a TALEN can be constructed with a DNA binding motif recognizing the desired nucleotide sequence[6]. When two TALENs are expressed in a cell and bind to the genome at an appropriate distance, called a spacer, the nuclease domain of FokI dimerizes and generates a double-strand break (DSB) within the spacer. The lesion is frequently repaired via nonhomologous end joining (NHEJ), an error-prone mechanism that results in the introduction of small insertion or deletion (indel) mutations. It has been reported that TALENs are useful for creating KO animals, such as fruitflies[9], silkworms[10], zebrafish[11–14], *Xenopus*[15,16] and rats[17,18]. Recently, it has been shown that TALEN technology can be

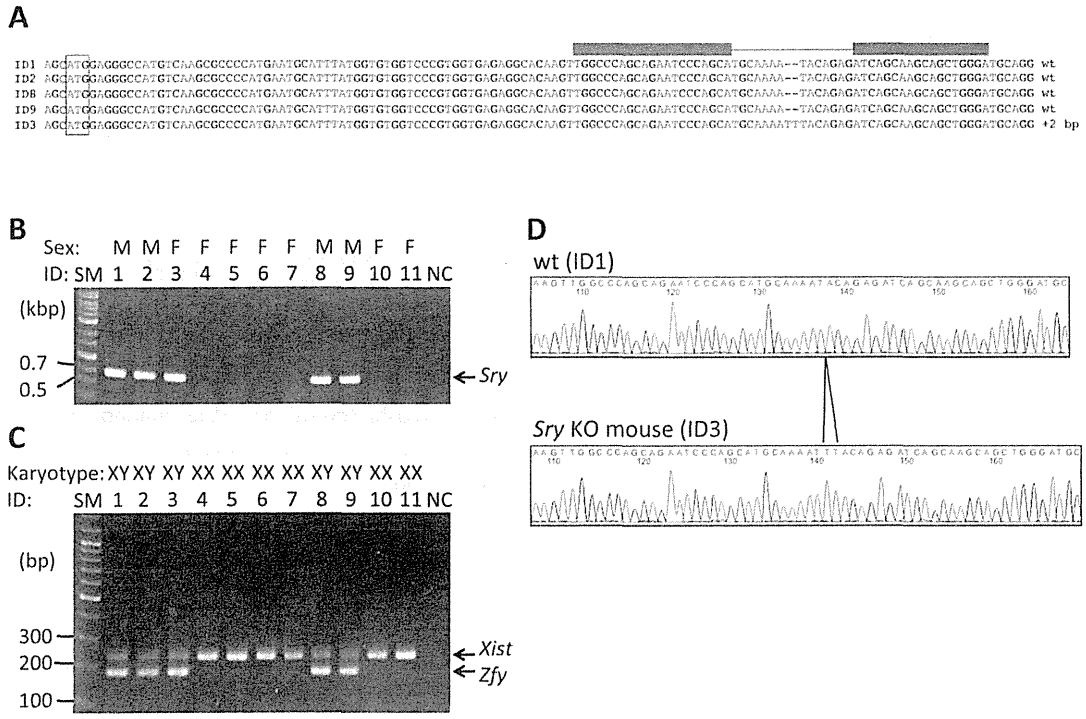

Figure 1 | Construction of the TALEN and generation of the *Sry* KO mouse. (A) Summary of the TALEN design and genotyping of the KO mouse. The positions of the TALEN targets and spacer are indicated by green boxes and a green line, respectively, above the nucleotide sequences. The blue box indicates the start codon of the *Sry* gene. ID of each mouse was shown at the left. Genotypes are indicated at the right. (B) Results of PCR amplification and agarose gel electrophoresis of *Sry*. M and F designate the phenotypic sex of male and female, respectively. DNA fragment lengths of the size markers are shown on the left. SM: size marker; NC: negative control. (C) Results of sexing PCR amplification and agarose gel electrophoresis. The karyotypes obtained from the experiment are shown at the top. DNA fragment lengths of the size markers are shown on the left. SM: size marker; NC: negative control. (D) Electropherograms around the TALEN spacer of the *Sry* KO (ID3) and wt male mice (ID1).

applied to generate autosomal gene KO mice via the microinjection of TALEN mRNA into fertilized oocytes[5,19,20]. TALEN can also be used to create Y-linked gene KO mice, as it recognizes specific sequences as short as approximately 45–65 nucleotides long.

In 2012, Wu et al.[21] reported the creation of a transgenic mouse in which *Sry* messenger RNA is knocked down *in vivo* using siRNA technology. In that report, the siRNA-treated developing gonads were feminized; however, it is difficult to knockdown target mRNA at 100% efficiency. Recently, the *Sry* gene was mutated using TALEN-mediated gene disruption in ES cells, and *Sry* KO mice were generated from the ES cells according to the tetraploid rescue method[22]. The authors reported that the *Sry* KO mice possessed sex reversed internal and external genitalia. In the current study, we generated *Sry* KO mouse using the microinjection of TALEN RNA into fertilized oocytes and present a detailed analysis of the KO mouse in regard to the hormone levels, histology of the gonads and brain, as well as gross morphology.

Results

Construction of TALEN and the production of *Sry* KO mouse. In order to generate *Sry* KO mouse, we adopted the TALEN-mediated method instead of the conventional homologous recombination-based ES cell modification strategy since *Sry* locates within 2.8 kb of a unique sequence at the center of a large inverted repeat structure[23]. The TALEN-mediated method is suitable for gene disruption of such repeat embedded genes and can be used to more quickly obtain KO mice since it can be applied to microinjection into oocytes, thereby bypassing gene targeting and chimera mouse generation using ES cells. To disrupt the *Sry* gene using TALEN, we set the TALEN recognition sequence at the 5′ part of the open reading frame (ORF) (Fig. 1A), so that almost the entire protein of SRY was lost due to a frameshift mutation once the TALEN caused an indel mutation. The TALEN RNAs were first microinjected into fertilized oocytes, then cultured at 37°C until transferred into pseudopregnant female mice (78% of the oocytes developed to the two-cell stage). PCR-sexing showed that 24 male pups were obtained out of 48 newborns, and PCR direct sequencing of *Sry* showed that no mutants were obtained (Table 1). It is possible that the optimal temperature for embryo culture, 37°C, is not suitable for TALEN. Therefore, we changed the temperature for the embryo culture to 30°C. This time, 129 oocytes were injected, 113 (88%) of which entered two-cell stage embryos (Table 1); therefore, the lower

Table 1 | Disruption of the *Sry* gene using TALEN technology

Temperature*	Injected	2-cell	Newborn	Males	Mutant
37°C	130	101 (78%)	48 (48%)	24 (50%)	0 (0%)
30°C	129	113 (88%)	23 (20%)	8 (35%)	1 (13%)

The percentages shown in parenthesis were derived from the number in the column as the numerator and the number in the column to the left as the denominator times 100.
*Temperature used for incubation after injection of the fertilized oocytes until transfer of the embryos into pseudopregnant females.

temperature of the embryo culture did not appear to hamper development. However, the ratio of delivered pups was reduced compared to that obtained when the injected oocytes were cultured at 37°C (Table 1). Based on visual inspection of sexual dimorphism of the external genitalia and the existence of nipples in the resulting pups obtained from the injected oocytes cultured at 30°C, we found that there were four males and seven females (Fig. 1B), whereas PCR genotyping in which the *Zfy* gene on the Y chromosome and the *Xist* gene on the X chromosome were amplified[24] showed that five mice had a Y chromosome (Fig. 1C), indicating that there was a sex reversal mouse (XY female, ID3). To investigate the effects of the TALEN, the flanking sequences of the TALEN target site on the *Sry* gene were amplified and sequenced (Fig. 1A, B,D). Four XY males had no mutations, while ID3 had two nucleotide insertions in the ORF of the *Sry* gene, causing a frameshift mutation (Fig. 1A, D). Our loss-of-function experiment with the *Sry* gene confirmed that *Sry* is the sex-determining gene on the Y chromosome, consistent with the findings of previous reports[3] utilizing gain-of-function experiments and the loss-of-function experiment of the *Sry* gene by Wang *et al.*[22] utilizing ES cells and the tetraploid rescue method.

External genitalia of the *Sry* KO mouse. The phenotype of the *Sry* KO mouse was examined in detail. Wild type females obtained at the same time as the KO mouse via microinjection were used as controls. The external genitalia of the *Sry* KO mouse at one and two months after birth was indistinguishable from that of the wt females (Fig. 2A). To compare the external genitalia of the *Sry* KO mouse and wt females in detail, we set out to observe the timing of vaginal opening and measure the anal-genital distance (AGD), an index of femaleness. If the sexual differentiation of the *Sry* KO mouse is not complete, it is possible that the vagina of the KO mouse would not be open, the timing of vaginal opening would be delayed and/or the AGD would not differ between males and females. We checked the timing of vaginal opening in three-week-old mice. There was little difference between the KO and wt female mice. The AGD was measured and normalized according to body weight at four and eight weeks of age, at which time, the AGD/body weight of the KO mouse was in the range of that of the wt females (Fig. 2B, C). These results suggest that the *Sry* KO mouse had a completely female type of external genitalia.

Internal genitalia of the *Sry* KO mouse. We next investigated the internal genitalia of the *Sry* KO mouse. The ovaries, oviducts and uterus in the *Sry* KO mouse were similar in size and morphology to those of the wt females (Fig. 3A–D). To compare the structure of the ovaries of the *Sry* KO mouse and wt females in detail, ovary sections were stained with hematoxylin and eosin (Fig. 3E–H). A few developing follicles, such as secondary and Graafian follicles, were observed (Fig. 3E, F) in both the wt and *Sry* KO ovaries; however, the number of follicles in the *Sry* KO ovaries was approximately half of that of the wt ovaries (Fig. 3J), and luteinizing had proceeded in the KO ovaries. In addition, it is noteworthy that luteinized unruptured follicles (LUFs), including oocytes retained in the corpus luteum, were observed in the *Sry* KO ovaries (Fig. 3I) but not in the wt ovaries. These results suggest that the *Sry* KO mouse had internal female genitalia; however, the ovaries were not completely the same as those of the wt females.

Hormone levels and the estrous cycle of the *Sry* KO mouse. In order to examine whether the *Sry* KO mouse had female type endocrinological features, the estrous cycle was investigated by smearing the vagina every morning at eight weeks of age. The *Sry* KO mouse exhibited a proestrus period for two days (Fig. 4A, B), followed by estrus for three days (Fig. 4C–E), metaestrus for one day (Fig. 4F) and diestrus for one day (Fig. 4G). Subsequently, the estrus cycle turned back to the proestrus period (Fig. 4H). The estrus period of the *Sry* KO mouse was a little longer than that of the wt females. Nonetheless, the estrus cycle of the *Sry* KO mouse was cycling. To confirm that the levels of sex hormones in the *Sry* KO mouse were in the range of females, the testosterone levels were measured. The blood plasma of four wt male mice obtained at the same time as the *Sry* KO mouse via microinjection, six wt females and the *Sry*

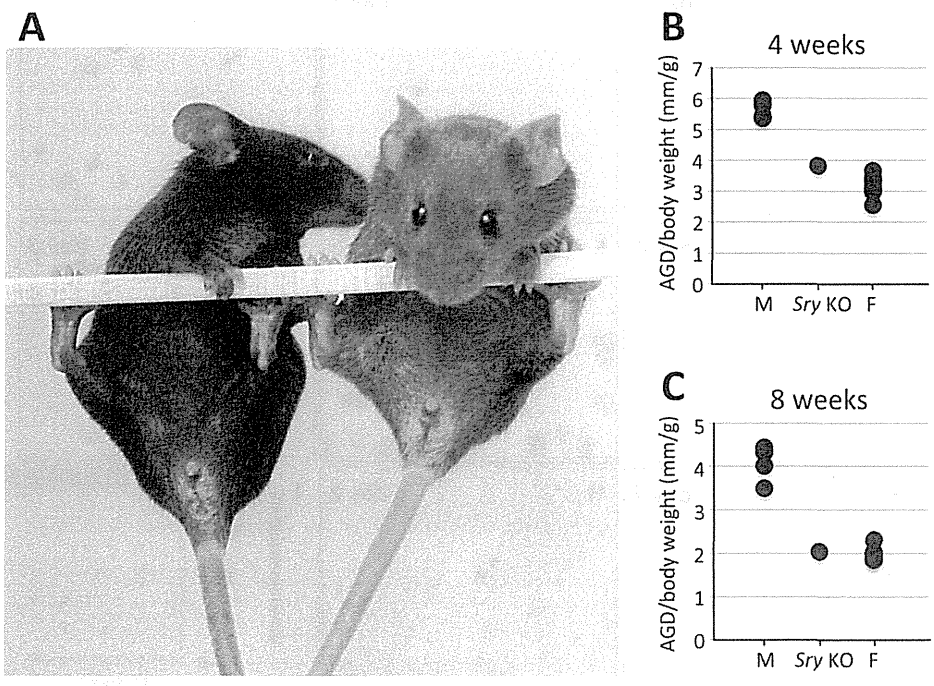

Figure 2 | External genitalia of the *Sry* KO mouse. (A) External genitalia of the *Sry* KO mouse. The photograph was taken in Animal Resources in National Research Institute for Child Health and Development by T.Kato and S.T. Left: *Sry* KO mouse; right: wt female mouse. (B) AGD normalized by body weight at four (top) and eight (bottom) weeks of age. Each dot shows the AGD/body weight of the individual mouse. M: male; F: female.

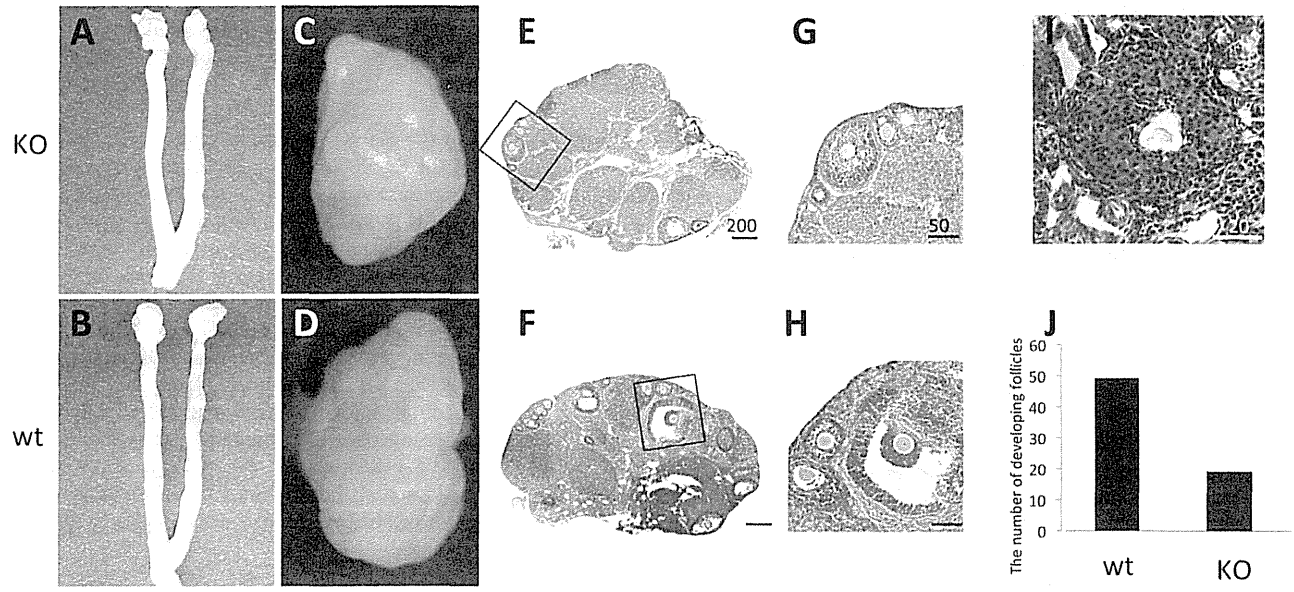

Figure 3 | Internal genitalia of the *Sry* KO mouse. (A), (B) Ovaries and uterus of the *Sry* KO mouse (A) and wt female (B). (C), (D) Ovaries of the *Sry* KO mouse (C) and wt female (D). (E–H) Ovarian cross-section of the *Sry* KO mouse (E), (G) and wt female (F, H). G and H are higher magnification images of areas within the rectangles in E and F, respectively. Scale bars in E and F = 200 μm. Scale bars in G and H = 50 μm. (I) LUFs in the *Sry* KO ovary. Scale bar = 20 μm. (J) Total numbers of counted developing follicles in the *Sry* KO mouse and wt female.

KO mouse were used. The testosterone levels were high in the wt males, whereas the testosterone levels in the females, including the *Sry* KO mouse, were below the confident limit (the levels in the four wt females were below the measurement limit) (Fig. 4I). This result shows that the testosterone level of the *Sry* KO mouse was in the range of those of the wt females.

Fertility of the *Sry* KO mouse. To examine the fertility of the *Sry* KO mouse, *Sry* KO mouse (nine weeks old) were mated with wt C57BL/6 male mouse, of which the fertility was confirmed before and after the experiment by mating with wt females, for four weeks. Although we confirmed the presence of the vaginal plug four times, pregnancy was not observed in the KO mouse, as we did not find any newborn pups

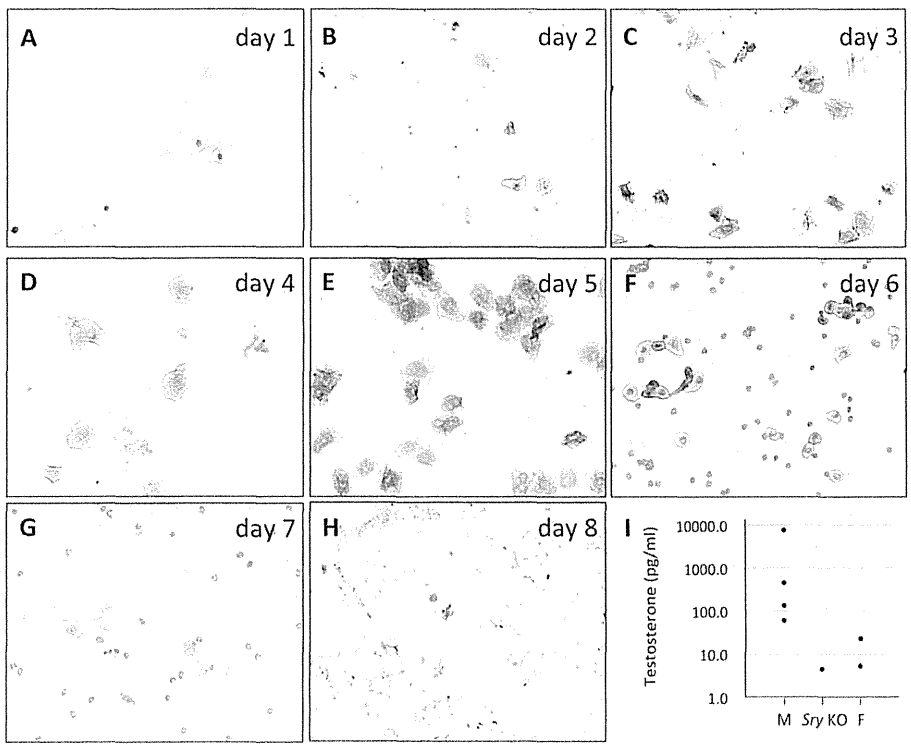

Figure 4 | Estrous cycle of the *Sry* KO mouse. Smear image of the *Sry* KO mouse. (A), (B), (H) Proestrus, (C–E) Estrus, (F) Metaestrus, (G) Diestrus. The day of the smear test is indicated on the top right in the image. (I) Testosterone levels of the *Sry* KO mouse. M: male; F: female.

or embryos at dissection at 14 weeks of age. This result implies that the *Sry* KO mouse was sterile or had reduced fertility, even though it had oocytes in their ovaries and performed copulatory behavior as females.

Brain of the *Sry* KO mouse. The *Sry* KO mouse demonstrated reproductive behavior when mated with the wt males, which prompted us to confirm whether the KO mouse had female type sexually dimorphic nuclei. The presence of a sexually dimorphic nucleus was determined in the medial preoptic area (MPOA) using staining with calbindin, with a higher number of immunoreactive cells observed in males[25]. We found that the number of calbindin expressing neurons in the anteroventral periventricular nucleus (AVPV) in the MPOA was higher in the wt male compared to that observed in the wt female (Fig. 5). In the *Sry* KO mouse, the number of calbindin expressing cells was equivalent to that observed in the wt female and lower than that observed in the wt male, especially in the medial dorsal portion. However, a small number of calbindin positive cells was detected in the ventromedial preoptic area of the AVPV, a finding that was relatively comparable to that observed in the wt male (Fig. 5).

Effect of *Sry* mutation on gene expression. In the end, we wanted to confirm whether functional SRY protein production was truly disrupted in our mutant mouse. However, since we obtained only one mutant mouse which did not produce an offspring, detection of the SRY protein in embryonic gonad, where it acts as sex determination factor, was technically impossible. Therefore we expressed wt and mutant *Sry* gene in cultured cell to confirm whether two nucleotide insertion that we observed in *Sry* KO mouse disrupts SRY protein production. Overexpression vector encoding ORF of *Sry* gene with or without the two nucleotide insertion were transfected to HEK-293T and protein products were detected by western blotting (Fig. 6B–D). Since *Sry* is an intronless gene, *Sry* ORF was obtained from PCR amplification using genomic DNA as a template. To facilitate the detection and to clarify which part of the gene is produced as protein, FLAG and S-tag were fused to N- and C- termini of *Sry*, in the reading frame of wt *Sry* ORF (i.e. C-terminal S-tag of mutant *Sry* construct is out of frame to the first methionine) (Fig. 6A). As shown in Fig. 6B and 6C, SRY protein containing FLAG and S-tag were detected from wt *Sry* expressed cells, whereas no signal was detected from mutant *Sry* expressed cells. This result suggested that *Sry* mutation we obtained actually disrupts SRY protein expression. We presume there could be two reasons why we did not detect any protein product from mutant *Sry* construct: first, mutated *Sry* transcript has premature stop codon and thus was degraded by nonsense-mediated mRNA decay. Alternatively, truncated SRY protein was indeed synthesized, but the expected protein is short and could be structurally unstable, and thus degraded by unfolded protein response, or too small to detect western blotting.

Discussion

We generated *Sry* KO mouse using TALEN RNA injection into fertilized oocytes. KO mice have been generated using ES cells via homologous recombination, which requires targeting vectors containing the homologous arm of several kilobases. This hampers the creation of KO mice of genes that are in or around repeat-rich regions, such as Y-linked genes. On the other hand, TALEN requires relatively short specific sequences for genome editing so that it can be used to create KO mice for genes within repeat-rich regions. Another advantage in using TALEN to make KO mice is that it enables KO mice to be obtained quickly when injected into fertilize oocytes because the time required to culture ES cells and produce chimera can be omitted.

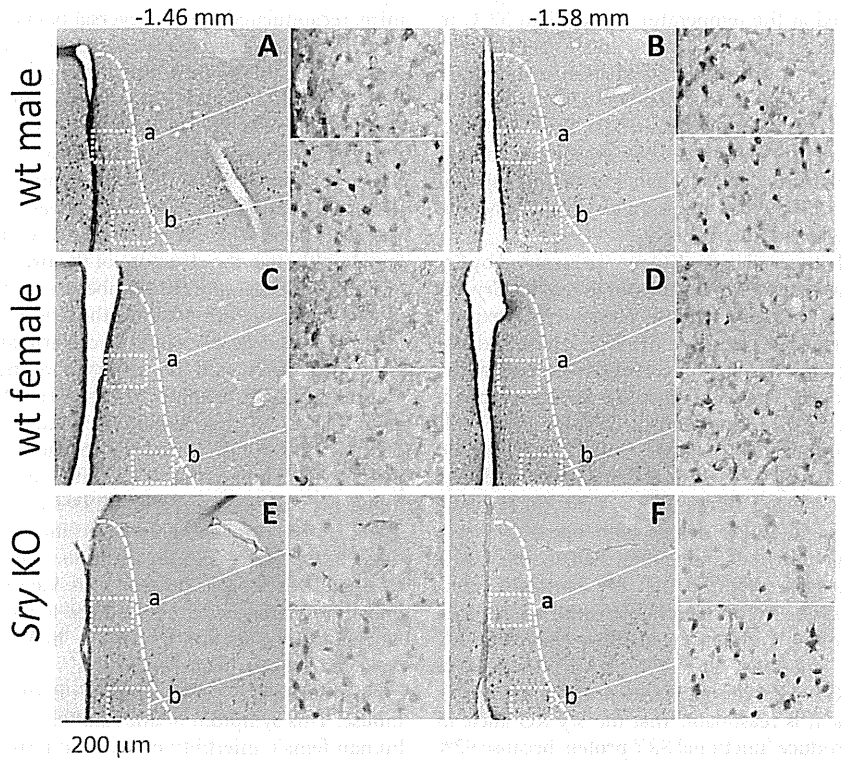

Figure 5 | Brain of the *Sry* KO mouse. Calbindin immunoreactive neurons were observed in the AVPV (dotted line) in the wt male (A, B), but not wt female (C), (D). The *Sry* KO mouse (E), (F) exhibited a lower expression level of calbindin in the medial dorsal portion of the AVPV compared to that observed in the wt male (square a); however, some positive cells were detected in the ventromedial preoptic area of the AVPV (square b). Scale bar = 200 μm.

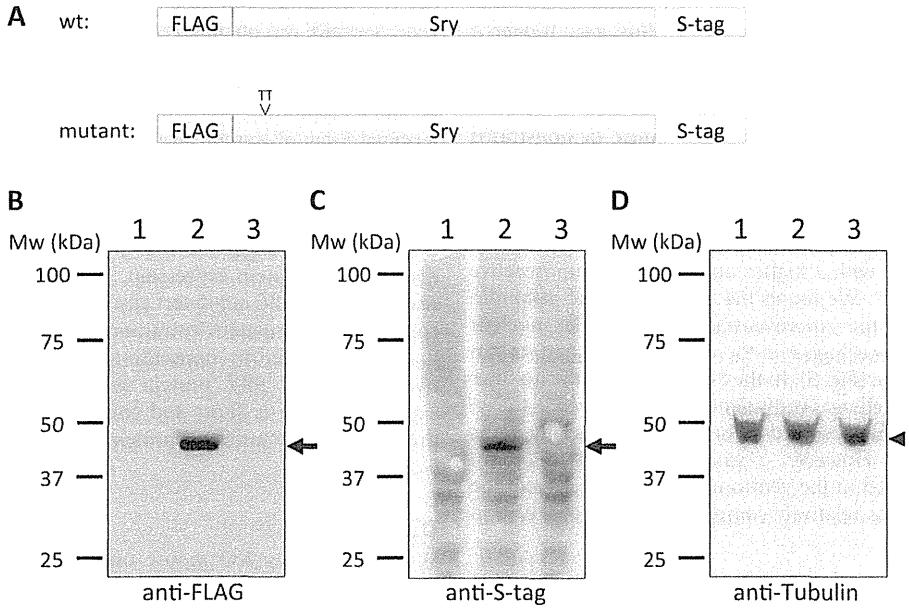

Figure 6 | Wild type and mutant *Sry* gene expression detected by western blotting. (A) Schematic representation of constructed gene structures in the expression vector. Position of the two nucleotide insertion (TT) is shown above the mutant gene structure. (B) Detection of wt and mutant SRY protein containing FLAG and S-tag at N- and C-termini, respectively, by western blotting using anti-FLAG antibody (arrow). Lane 1: empty vector transfected cell lysate; lane 2: wt *Sry* with FLAG and S-tag; lane3: mutant *Sry* with FLAG and S-tag. Size marker is shown at left of image. (C) Detection of wt and mutant SRY protein containing FLAG and S-tag at N- and C-termini, respectively, by western blotting using anti-S-tag antibody (arrow). Lanes and markers are same as those of (B). (D) Detection of tubulin by western blotting (arrowhead) as a control for amount of protein loading. Lanes and markers are same as those of (B).

We could not obtain *Sry* KO mouse by incubation of TALEN RNA injected oocytes incubated at 37°C. Since successful mutagenesis using TALEN was reported at the temperature lower than 37°C in heterothermic animals such as fruit flies[9], silkworms[10], zebrafish[11–14] and *Xenopus*[15,16], we thought lowering the incubation temperature could ameliorate the mutagenesis rate. Thus we incubate TALEN RNA injected oocytes at 30°C and could obtained the *Sry* KO mouse. We cannot conclude which temperature is better for making knockout mouse using TALEN from our data, but incubating injected oocyte at 30°C could be an option for whom cannot obtain knockout mouse when injected oocytes are incubated at 37°C.

To evaluate sex reversal observed in *Sry* KO mouse is caused by *Sry* gene mutation, the best way is rescue of the phenotypes of the *Sry* KO mouse by crossing with *Sry* transgenic mouse. However this experiment could not be performed because the *Sry* KO mouse did not produce an offspring. We introduced a dinucleotide insertion at the 5′ part of the ORF of the *Sry* gene, so that the protein product contains 32 intact amino acid residues (intact deduced SRY (RefSeq: NM_011564): 395 amino acid residues) with 30 new amino acids or mRNA is degraded by nonsense-mediated mRNA decay. In the former case the expected mutant SRY lacks functionally important motifs, such as a glutamine-rich domain, one of two nuclear localization signals (NLSs) and more than half of the HMG domain. Previous studies have reported that *Sry* transgenic constructs without the glutamine-rich domain fail to cause sex reversal in mice with the XX karyotype[26], mutations in either NLS cause XY sex reversal in humans[27–30] and most cases of human XY sex reversal involve mutations in HMG box (review in Harley and Goodfellow[31]). Considering these reports, it is reasonable that the *Sry* KO allele in our KO mouse does not produce functional SRY protein because 92% of the ORF was not translated and functionally important motifs were located on the missing residues.

In the present study, we analyzed the effects of *Sry* gene depletion in XY mouse. Recently Wang *et al*[22] reported *Sry* KO mouse created through TALEN mediated gene disruption in ES cells. They showed the KO mouse had female type genitalia and reduced fertility. Our KO mouse, which had different mutant allele to previously reported mice, recapitulated the sex reversal phenotype which confirmed the fundamental role of *Sry* gene for male sex determination. Moreover, in this study we provided the histological and physiological phenotypes of *Sry* KO mouse. The external and internal genitalia were, as expected, female, the testosterone levels were within the female range, the estrous cycle was the same as that of the wt females, the copulatory behavior was the same as that of females and the dimorphic nucleus in the AVPV was of the female type. These results indicate that *Sry* KO mouse is sex reversed and healthy female, although the structure of the ovaries was different from that of normal females and the number of oocytes was reduced. We were unable to distinguish whether the *Sry* KO mouse had reduced fertility or was sterile, although we confirmed the presence of a vaginal plug four times, and no embryos or newborns were identified. Considering that Wang *et al.*[22] reported that *Sry* KO mice created using ES cell KO and tetraploid rescue have reduced fertility, it is possible that our KO mouse also had reduced fertility. If so, it is possible that the number of ovulated mature oocytes in the *Sry* KO mouse was reduced. Indeed, the ovaries of the *Sry* KO mouse contained fewer developing follicles and were more luteinized than those of the wt females. In addition, a few LUFs, including oocytes retained in the corpus luteum, were identified in the *Sry* KO ovaries only. In humans, LUFs are observed in 5–10% of menstrual cycles of normal fertile females[32], while a higher incidence of LUFs has been reported in infertile females[33]. In the latter cases, an estrous cycle is normal[33–35]. This situation is similar to that of the *Sry* KO mouse. This symptom of anovulation is considered to be a cause of human female infertility or reduced fertility[35]. However, we do not know whether the LUFs observed in the *Sry* KO mouse were caused by the existence of the Y chromosome or dysfunction of the ovaries. If the latter case is true, then it is possible that *Sry* KO mouse could be used as a model for infertility or reduced fertility containing LUFs.

We found that the *Sry* KO mouse demonstrated female-like calbindin positive cells in the MPOA, especially in the medial dorsal portion of the AVPV. The distribution patterns of the calbindin expressing neurons in the wt males were different from the findings of a previous report of C57/BL6 males[25]. This is likely due to the difference in mouse strains[36]. In fact, clear sex differences in the number of calbindin expressing neurons were observed in the MPOA in this B6CBAF1/J strain in the medial dorsal portion of the AVPV, in which many Kisspeptin containing neurons exist. Kisspeptin neurons in the AVPV stimulate GnRH secretion[37], which results in an increase in female copulatory behavior[38]. Interestingly, the *Sry* KO mouse exhibited female-like calbindin expressing neurons in the AVPV, suggesting that this female-like AVPV structure is related to the normal female-type copulatory behavior observed in the *Sry* KO mouse. However, a small number of calbindin positive cells was detected in the ventromedial preoptic area of the AVPV in the *Sry* KO mouse, which was relatively comparable to that observed in the wt male (Fig. 6). The neurons in the ventromedial preoptic area of the AVPV are related to the onset of anestrous in ewes[39] and project to and stimulate hypothalamus dopaminergic neurons[40]. A higher level of dopaminergic activity blocks pregnancy by decreasing the release of prolactin from the pituitary[41]. Therefore, the male-like structure of the ventromedial preoptic area of the AVPV may be related to the prolonged estrous cycle and reduced fertility observed in the *Sry* KO mouse. It is unclear why MPOA was not fully reversed from a male- to female-type structure in the *Sry* KO mouse. One possibility is a parent-of-origin imprinting gene expression in the hypothalamus. In the hypothalamus, sex-specific imprinted genes are found in females, which suggests a parental allelic influence over the hypothalamic function in XX females[42]. Therefore, *Sry* KO mouse lacked some female functions in the hypothalamus.

Methods

TALEN. The TALEN plasmids were designed using the online TAL Effector Nucleotide Targeter 2.0 software program (https://tale-nt.cac.cornell.edu/node/add/talen-old) with the following parameters: Minimum Spacer Length at 12 bp, Maximum Spacer Length at 16 bp, Minimum Repeat Array Length at 16 and Maximum Repeat Array Length at 20. The query sequence used was the reverse complementary sequence of nucleotide number 1919368–1919568 on chromosome Y (Assembly by July 2007 (NCBI37/mm9)). Position 1 of the query sequence corresponds to the initiation codon of the *Sry* gene. One of the possible TALEN target sequences identified by the program was selected empirically. The TALENs were assembled in pcDNA-TAL-NC vector plasmids using a previously described protocol[43]. A Golden Gate TALEN and TAL Effector Kit was obtained from Addgene[44]. The target sequences of the *Sry* TALENs were as follows: left 5′-TGG CCC AGC AGA ATC CCA GCA-3′ and right 5′-TCC CAG CTG CTT GCT GAT-3′.

Microinjection. TALEN plasmids were digested by PvuII restriction endonuclease. One microgram of the digested plasmids was used as a template for the *in vitro* transcription reaction using the mMESSAGE mMACHINE T7 Kit (Life Technologies) according to the manufacturer's instructions. The synthesized RNAs were purified using the MegaClear kit (Life Technologies) according to the manufacturer's instructions. The RNA concentration was determined using a NanoDrop 1000 spectrophotometer and diluted with injection buffer (10 mM Tris-HCl/0.1 mM EDTA (pH 7.4)) at 600 ng/μl in a total of two TALEN mRNAs (1 : 1 ratio, i.e. 300 ng/μl each). The microinjection of the two TALEN mRNAs mix into cytoplasm of pronuclear stage oocytes was carried out under standard procedures using oocytes obtained from superovulated (C57BL/6 × DBA2) F1 mice mated with male mice of the same strain (Sankyo Labo Service Corporation). The injected oocytes were cultured in M16 medium at 30 or 37°C. The following day, embryos developed into the two-cell stage were transferred into pseudopregnant ICR female mice. All animal care protocols and experiments were approved by the Animal Care and Use Committee at the National Research Institute for Child Health and Development.

PCR-based genotyping and sexing. Genomic DNA was extracted from tail tips using amputation. For genotyping of *Sry*, PCR was carried out using the following primers: SryF475 (5′- CTG TCC CAC TGC AGA AGG TT -3′) and SryR412 (5′- GGG CTG GAC TAG GGA GGT CCT G -3′). The PCR products were treated with ExoSAP-IT (Affymetrix) and used as templates for sequencing. The sequencing primer was SrySeq476 (5′- CAG CCC TAC AGC CAC ATG AT -3′). For PCR-based sexing, the Y chromosome-specific gene, *Zfy*, and the X chromosome-specific gene, *Xist*, were amplified using the primer set described by Obata *et al.*[24].

Vaginal smear test. The estrous cycle was analyzed using a vaginal smear test. *Sry* KO mouse and wt females (eight weeks of age) were used for eight successive days. Every morning, PBS was applied to the vagina and pipetted well. The liquid was collected and uniformly smeared on a slide glass. The samples were air dried, fixed in methanol, stained with Giemsa solution and washed in tap water. The specimens were micrographed using an optical microscope.

Fertility check. Female mice nine weeks of age were mated with wt C57BL/6 male mice, of which fertility was confirmed by crossing with C57BL/6 females before and after crossing with the *Sry* KO mouse. The presence of the vaginal plug and parturition were checked every morning for four weeks.

Hormone assay. The mice were anesthetized, and blood was collected from the heart before euthanasia. The blood plasma was separated immediately after collection and stored at −80°C. The hormones levels were analyzed using a radioimmunoassay which was performed by Asuka Pharmaceutical Co., Ltd.

Histology. The mice were perfusion fixed through the heart using 4% paraformaldehyde. The brains and gonads were collected and embedded in paraffin. The embedded ovary paraffin block was sectioned at 6 μm. Deparaffinized sections were stained with hematoxylin and eosin. Six representative sections with more than 75 μm of distance between each other were chosen, and the numbers of developing follicles, including secondary follicles and Graafian follicles, per ovarian cross section were counted. As to calbindin immunohistochemistry, sections containing the MPOA (−0.5 to −1.8 mm from bregma) were sectioned at 30 μm. One of two sequential sections was subjected to immunohistochemistry. The staining methods have been previously described[25]. Briefly, the sections were incubated with the first monoclonal antibody to calbindin (C9848-2ML; Sigma-Aldrich, 1 : 12000) for 48 hours. After rinsing, the sections were incubated with biotinylated horse anti-mouse IgG antibodies (BA-2000, Vector Lab, 1 : 500), then reacted with the ABC kit (VECTASTAIN Elite ABC kit, Vector Labs).

Transfection and western blotting. ORF of *Sry* was PCR amplified using genomic DNA purified from wt male and *Sry* KO mouse using primers SryORF XhoI-FLAG F (5′- gcc tcg agA TGG ACT ACA AGG ACG ATG ATG ACA AGG GCa tgg agg gcc atg tca agc g-3′), where XhoI recognition site and FLAG tag indicated with underline and capital letters, respectively, and SryORF EcoRI StagR (5′- gcg aat tct caG CTG TCC ATG TGC TGT CTC TCG AAC TTG GCA GCG GCG GTC TCC TTt gag act gcc aac cac agg g-3′), where EcoRI recognition site and FLAG tag indicated with underline and capital letters, respectively. PCR products were cloned in pIRES2-EGFP (Clontech) using EcoRI/XhoI. Plasmids were transfected to HEK-293T cell using Fugene HD (Promega) according to the manufacturer's instruction. After 48 hours incubation at 37°C, transfection efficiency was confirmed by checking EGFP emission and cells were lysed with cell lysis buffer (50 mM HEPES [pH 7.8], 200 mM NaCl, 5 mM EDTA, 1% NP40, 5% glycerol, freshly complemented with 1 mM DTT, protease inhibitor cocktail (Roche)). The cell lysate was analyzed by western blotting using 10% SDS-PAGE, Immobilon PVDF memmbrane (Millipore), monoclonal anti-FLAG M2 antibody (SIGMA), anti-S-tag antibody (Abcam), anti-mouse IgG HRP conjugated (SIGMA), anti-rabbit IgG HRP conjugated (SIGMA) and ECL (GE).

1. Gubbay, J. *et al.* A gene mapping to the sex-determining region of the mouse Y chromosome is a member of a novel family of embryonically expressed genes. *Nature* **346**, 245–250 (1990).
2. Koopman, P., Münsterberg, A., Capel, B., Vivian, N. & Lovell-Badge, R. Expression of a candidate sex-determining gene during mouse testis differentiation. *Nature* **348**, 450–452 (1990).
3. Koopman, P., Gubbay, J., Vivian, N., Goodfellow, P. & Lovell-Badge, R. Male development of chromosomally female mice transgenic for Sry. *Nature* **351**, 117–121 (1991).
4. Hawkins, J. R. *et al.* Mutational analysis of SRY: nonsense and missense mutations in XY sex reversal. *Hum Genet* **88**, 471–474 (1992).
5. Sung, Y. H. *et al.* Knockout mice created by TALEN-mediated gene targeting. *Nat Biotechnol* **31**, 23–24 (2013).
6. Christian, M. *et al.* Targeting DNA double-strand breaks with TAL effector nucleases. *Genetics* **186**, 757–761 (2010).
7. Boch, J. *et al.* Breaking the code of DNA binding specificity of TAL-type III effectors. *Science* **326**, 1509–1512 (2009).
8. Moscou, M. J. & Bogdanove, A. J. A simple cipher governs DNA recognition by TAL effectors. *Science* **326**, 1501 (2009).
9. Liu, J. *et al.* Efficient and specific modifications of the Drosophila genome by means of an easy TALEN strategy. *J Genet Genomics* **39**, 209–215 (2012).
10. Ma, S. *et al.* Highly efficient and specific genome editing in silkworm using custom TALENs. *PLoS One* **7**, e45035 (2012).
11. Huang, P. *et al.* Heritable gene targeting in zebrafish using customized TALENs. *Nat Biotechnol* **29**, 699–700 (2011).
12. Sander, J. D. *et al.* Targeted gene disruption in somatic zebrafish cells using engineered TALENs. *Nat Biotechnol* **29**, 697–698 (2011).
13. Bedell, V. M. *et al.* In vivo genome editing using a high-efficiency TALEN system. *Nature* **491**, 114–118 (2012).

14. Cade, L. *et al.* Highly efficient generation of heritable zebrafish gene mutations using homo- and heterodimeric TALENs. *Nucleic Acids Res* **40**, 8001–8010 (2012).
15. Lei, Y. *et al.* Efficient targeted gene disruption in Xenopus embryos using engineered transcription activator-like effector nucleases (TALENs). *Proc Natl Acad Sci U S A* **109**, 17484–17489 (2012).
16. Suzuki, K. I. *et al.* High efficiency TALENs enable F0 functional analysis by targeted gene disruption in Xenopus laevis embryos. *Biology Open* **2**, 448–452 (2013).
17. Tesson, L. *et al.* Knockout rats generated by embryo microinjection of TALENs. *Nat Biotechnol* **29**, 695–696 (2011).
18. Mashimo, T. *et al.* Efficient gene targeting by TAL effector nucleases coinjected with exonucleases in zygotes. *Sci Rep* **3**, 1253 (2013).
19. Davies, B. *et al.* Site Specific Mutation of the Zic2 Locus by Microinjection of TALEN mRNA in Mouse CD1, C3H and C57BL/6J Oocytes. *PLoS One* **8**, e60216 (2013).
20. Qiu, Z. *et al.* High-efficiency and heritable gene targeting in mouse by transcription activator-like effector nucleases. *Nucleic Acids Res* **41**, e120 (2013).
21. Wu, N., Yu, A.-B., Zhu, H.-B. & Lin, X.-K. Effective silencing of Sry gene with RNA interference in developing mouse embryos resulted in feminization of XY gonad. *J Biomed Biotechnol* **2012**, 343891 (2012).
22. Wang, H. *et al.* TALEN-mediated editing of the mouse Y chromosome. *Nat Biotechnol* **31**, 530–532 (2013).
23. Gubbay, J. *et al.* Inverted repeat structure of the Sry locus in mice. *Proc Natl Acad Sci U S A* **89**, 7953–7957 (1992).
24. Obata, Y. *et al.* Post-implantation development of mouse androgenetic embryos produced by in-vitro fertilization of enucleated oocytes. *Hum Reprod* **15**, 874–80 (2000).
25. Orikasa, C. & Sakuma, Y. Estrogen configures sexual dimorphism in the preoptic area of C57BL/6J and ddN strains of mice. *J Comp Neurol* **518**, 3618–3629 (2010).
26. Bowles, J., Cooper, L., Berkman, J. & Koopman, P. Sry requires a CAG repeat domain for male sex determination in Mus musculus. *Nat Genet* **22**, 405–408 (1999).
27. Battiloro, E. *et al.* A novel double nucleotide substitution in the HMG box of the SRY gene associated with Swyer syndrome. *Hum Genet* **100**, 585–587 (1997).
28. Veitia, R. *et al.* Mutations and sequence variants in the testis-determining region of the Y chromosome in individuals with a 46,XY female phenotype. *Hum Genet* **99**, 648–652 (1997).
29. Harley, V. R. *et al.* Defective importin beta recognition and nuclear import of the sex-determining factor SRY are associated with XY sex-reversing mutations. *Proc Natl Acad Sci U S A* **100**, 7045–7050 (2003).
30. Sim, H. *et al.* Defective calmodulin-mediated nuclear transport of the sex-determining region of the Y chromosome (SRY) in XY sex reversal. *Mol Endocrinol* **19**, 1884–1892 (2005).
31. Harley, V. R. & Goodfellow, P. N. The biochemical role of SRY in sex determination. *Mol. Reprod Dev* **39**, 184–193 (1994).
32. Killick, S. & Elstein, M. Phamacologic production of lutenized unruptured follicles by prostaglandin synthetase inhibitors. *Fertil Steril* **47**, 773–777 (1987).
33. Marik, J. & Hulka, J. Lutenized unruptured follicle syndrome; a subtle cause of infertility. *Fertil Steril* **29**, 270–274 (1978).
34. Hamilton, C. J. *et al.* Follicle growth curves and hormonal patterns in patients with the lutenized unruptured follicle syndrome. *Fertil Steril* **43**, 541–548 (1985).
35. LeMaire, G. S. The lutenized unruptured follicle syndrome: anovulation in disguise. *J. Obstet. Gynecol. Neonatal Nurs* **16**, 116–120 (1987).
36. Mathieson, W. B., Taylor, S. W., Marshall, M. & Neumann, P. E. Strain and sex differences in the morphology of the medial preoptic nucleus of mice. *J Comp Neurol* **428**, 254–265 (2000).
37. Messager, S. *et al.* Kisspeptin directly stimulates gonadotropin-releasing hormone release via G protein-coupled receptor 54. *Proc. Natl Acad Sci U S A* **102**, 1761–1766 (2005).
38. Keller, M., Pierman, S., Douhard, Q., Baum, M. J. & Bakker, J. The vomeronasal organ is required for the expression of lordosis behaviour, but not sex discrimination in female mice. *Eur J Neurosci* **23**, 521–530 (2006).
39. Anderson, G. M. *et al.* Evidence that thyroid hormones act in the ventromedial preoptic area and the premammillary region of the brain to allow the termination of the breeding season in the ewe. *Endocrinology* **144**, 2892–2901 (2003).
40. Anderson, G. M., Connors, J. M., Hardy, S. L., Valent, M. & Goodman, R. L. Oestradiol microimplants in the ventromedial preoptic area inhibit secretion of luteinizing hormone via dopamine neurones in anoestrous ewes. *J Neuroendocrinol* **13**, 1051–1058 (2001).
41. Rosser, A. E., Remfry, C. J. & Keverne, E. B. Restricted exposure of mice to primer pheromones coincident with prolactin surges blocks pregnancy by changing hypothalamic dopamine release. *J Reprod Fertil* **87**, 553–559 (1989).
42. Gregg, C., Zhang, J., Butler, J. E., Haig, D. & Dulac, C. Sex-specific parent-of-origin allelic expression in the mouse brain. *Science* **329**, 682–685 (2010).
43. Sakuma, T. *et al.* Efficient TALEN construction and evaluation methods for human cell and animal applications. *Genes Cells* **18**, 315–326 (2013).
44. Cermak, T. *et al.* Efficient design and assembly of custom TALEN and other TAL effector-based constructs for DNA targeting. *Nucleic Acids Res* **39**, e82 (2011).

Acknowledgments

We would like to thank Maki Fukami for thoughtful discussion and critical reading of the manuscript, Yuko Katoh-Fukui and Kenji Miyado for helpful discussion and Mami Miyado for instructions regarding AGD measurement. This work was supported, in part, by The Grant of National Center for Child Health and Development, Grant Number 25-1, JSPS KAKENHI Grant Number 24115707 and JST (CREST) for H.A. and JSPS KAKENHI Grant Number 25132713 and MEXT KAKENHI Grant Number 23570265 and The Grant of National Center for Child Health and Development, Grant Number 24-3 for S.T.

Author contributions

K.Miyata, S.Y., S.M. and S.T. constructed the TALEN plasmids, T.S. and T.Y. provided instructions regarding the construction of the TALEN plasmids, M.T. performed the microinjection experiments, M.S. and T. Kikusi carried out the detection of the dimorphisms in the brain, S.Y., M.I., K.Miura. and Y.K. performed detection of SRY protein, T. Kato and S.T. conducted the remainder of the experiments, M.I., H.A. and S.T. designed the project and S.T. wrote the paper. All authors discussed the results and commented on the manuscript.

Additional information

Competing financial interests: The authors declare no competing financial interests.

How to cite this article: Kato, T. *et al.* Production of *Sry* knockout mouse using TALEN via oocyte injection. *Sci. Rep.* 3, 3136; DOI:10.1038/srep03136 (2013).

Published OnlineFirst November 22, 2013; DOI: 10.1158/0008-5472.CAN-13-1836

Cancer Research

Small Molecule Agonists of PPAR-γ Exert Therapeutic Effects in Esophageal Cancer

Hiroshi Sawayama, Takatsugu Ishimoto, Masayuki Watanabe, et al.

Cancer Res 2014;74:575-585. Published OnlineFirst November 22, 2013.

Published OnlineFirst November 22, 2013; DOI: 10.1158/0008-5472.CAN-13-1836

Cancer Research

Small Molecule Agonists of PPAR-γ Exert Therapeutic Effects in Esophageal Cancer

Hiroshi Sawayama[1], Takatsugu Ishimoto[1], Masayuki Watanabe[1], Naoya Yoshida[1], Hidetaka Sugihara[1], Junji Kurashige[1], Kotaro Hirashima[1], Masaaki Iwatsuki[1], Yoshifumi Baba[1], Eiji Oki[2], Masaru Morita[2], Yoshinobu Shiose[3], and Hideo Baba[1]

Abstract

The transcription factor PPAR-γ plays various roles in lipid metabolism, inflammation, cellular differentiation, and apoptosis. PPAR-γ agonists used to treat diabetes may have utility in cancer treatment. Efatutazone is a novel later generation PPAR-γ agonist that selectively activates PPAR-γ target genes and has antiproliferative effects in a range of malignancies. In this study, we investigated PPAR-γ status in esophageal squamous cell carcinoma (ESCC) and investigated the antiproliferative effects of efatutazone. PPAR-γ was expressed heterogeneously in ESCC, in which it exhibited an inverse relationship with Ki-67 expression. PPAR-γ expression was associated independently with good prognosis in ESCC. Efatutazone, but not the conventional PPAR-γ agonist troglitazone, inhibited ESCC cell proliferation *in vitro* and *in vivo*. Mechanistic investigations suggested that efatutazone acted by upregulating p21Cip1 protein in the nucleus through inactivation of the Akt pathway and dephosphorylation of p21Cip1 at Thr145 without affecting the transcriptional activity of p21Cip1. We also found that treatment with efatutazone led to phosphorylation of the EGF receptor and activation of the mitogen-activated protein kinase (MAPK) pathway. Accordingly, the combination of efatutazone with the antiepithelial growth factor receptor antibody cetuximab synergized to negatively regulate the phosphoinositide 3-kinase–Akt and MAPK pathways. Together, our results suggest that efatutazone, alone or in combination with cetuximab, may offer therapeutic effects in ESCC. *Cancer Res; 74(2); 575–85. ©2013 AACR.*

Introduction

PPAR-γ is a member of the nuclear hormone receptor superfamily of ligand-activated transcription factors (1). PPAR-γ plays a variety of roles in adipose cell differentiation, modulation of metabolism, and the inflammatory response (2, 3). The protein interacts with and/or regulates multiple signaling pathways, including those associated with p21Cip1 (4, 5) and p27 (6, 7) to regulate the cell cycle, with nuclear factor kappa β (8) to reduce the expression of cytokines such as interleukin-6, and interleukin-8, and with cyclooxygenase-2 and prostaglandin E2 to suppress inflammation (9, 10). Genetic studies have indicated that PPAR-γ functions as a tumor suppressor in a variety of tissues, including the breast (11), prostate (12), and colon (13).

Ligands for PPAR-γ include endogenous ligands such as fatty acids, $\Delta^{12,15}$ prostaglandin J2 (14), and exogenous ligands, such as the thiazolidinedione class of antidiabetic drugs including troglitazone, rosiglitazone, and pioglitazone (15, 16). Numerous recent studies have demonstrated that PPAR-γ ligands exert antiproliferative effects. The first-generation thiazolidinedione troglitazone showed antiproliferative effects in hepatocellular carcinoma (7), colorectal cancer (17, 18), and breast cancer (19). However, these effects were limited, and small clinical trials showed no beneficial effects of these conventional PPAR-γ ligands (20, 21).

Efatutazone is a novel third-generation thiazolidinedione PPAR-γ agonist, which is at least 500-fold more potent than troglitazone in terms of PPAR response-element activation and inhibition of cancer cell growth, rather than inducing apoptosis (4). Furthermore, efatutazone demonstrated antitumor effects in patients with advanced malignancies (22). This agent therefore shows great potential for practical cancer therapy.

Combination therapy using efatutazone with antitumor agents represents an important means of achieving significant tumor regression (22). PPAR-γ agonists have shown activity both *in vitro* and *in vivo* in combination with conventional anticancer drugs including platinum-based drugs (23), taxanes (4), and irinotecan (24). However, the pathways affected by

Authors' Affiliations: [1]Department of Gastroenterological Surgery, Graduate School of Medical Sciences, Kumamoto University, Kumamoto; [2]Department of Surgery and Science, Graduate School of Medical Sciences, Kyushu University, Fukuoka; and [3]Research and Development Division, Daiichi Sankyo Co., Ltd., Tokyo, Japan

Note: Supplementary data for this article are available at Cancer Research Online (http://cancerres.aacrjournals.org/).

H. Sawayama and T. Ishimoto contributed equally to this work.

Corresponding Author: H. Baba, Department of Gastroenterological Surgery, Graduate School of Medical Sciences, Kumamoto University, 1-1-1 Honjo, Kumamoto 860-8556, Japan. Phone: 81-96-373-5587; Fax: 81-96-373-4378; E-mail: hdobaba@kumamoto-u.ac.jp

doi: 10.1158/0008-5472.CAN-13-1836

Published OnlineFirst November 22, 2013; DOI: 10.1158/0008-5472.CAN-13-1836

treatment with efatutazone, and the most suitable combination therapy (in terms of molecular-targeted agents) based on theoretical signaling mechanisms remain unclear.

Esophageal carcinoma affects more than 450,000 people worldwide, and its incidence is increasing rapidly. SCC is the predominant form of esophageal carcinoma worldwide (25). Furthermore, esophageal carcinoma is an aggressive disease with a propensity to spread both locoregionally and distally, and multidisciplinary therapy has therefore been tested for esophageal squamous cell carcinoma (ESCC; refs. 26, 27). The antiepithelial growth factor receptor (EGFR) antibody, cetuximab, was approved for head and neck SCC (28, 29), and new molecular-targeted therapies have been expected for the treatment of ESCC (30).

The effects of PPAR-γ are tissue and cancer specific. The significance of PPAR-γ expression and antiproliferative effects of PPAR-γ agonists in ESCC have been reported in a few studies, however these studies were limited because they only evaluated the mRNA levels in small number of samples (31), in adenocarcinomas (32), or using conventional PPAR-γ agonists, such as troglitazone (33). Therefore the expression of the PPAR-γ protein in ESCC and the antiproliferative effects of the new generation PPAR-γ agonist remained unclear. In this study, we investigated the relationship between the expression levels of PPAR-γ and Ki-67 in patients with ESCC, and examined the antiproliferative effects and underlying mechanism of efatutazone monotherapy both *in vitro* and *in vivo*. We also investigated the effects of combination therapy using efatutazone with molecular-targeted agents, based on signaling analysis. The results of this study may provide a novel therapeutic strategy for ESCC, and suggest that efatutazone, both alone and in combination with an anti-EGFR antibody, may improve the outcomes of patients with ESCC.

Materials and Methods

Chemicals

Efatutazone was kindly provided by Daiichi Sankyo, Inc.. Troglitazone, U0126, MK-2206 dihydrochloride, and cetuximab were purchased from Cayman, Wako, Selleck Bio., and Kumamoto University Hospital, respectively. For the *in vitro* analyses, efatutazone was prepared in dimethyl sulfoxide (DMSO) before addition to cell cultures. Antibody information is provided in the Supplementary Materials and Methods.

Patients

This study involved 145 consecutive patients who underwent surgical resection of ESCC at Kumamoto University Hospital from January 2000 to December 2008 (Supplementary Fig. S1).

Cell lines

ESCC cell lines (TE series) and HT-29 were obtained from Cell Resource Center for Biomedical Research Institute of Development, Aging and Cancer, Tohoku University, the Riken BioResource Center Cell Bank, and Keio University. The cell lines have been tested and authenticated by Cell ID System in October 2013. Cell lines (TE series and HT-29) were cultured in 5% CO_2 at 37°C in RPMI 1640 supplemented with 10% FBS.

Xenograft model

Six-week-old nude mice (Balb-nu/nu slc) were inoculated subcutaneously in the right flank with 5×10^6 TE-4 cells in 200 mL PBS containing 50% Matrigel (BD, Becton, Dickinson and Company). When the tumors reached approximately 80 mm^3 in diameter, the mice were randomized into treatment groups. This subcutaneous xenograft model was used to assess the therapeutic effects of efatutazone (10 mg/kg) and troglitazone (10 mg/kg) as single agents. Control animals received 0.5 w/v% methylcellulose solution (vehicle). Efatutazone and troglitazone were suspended in 0.5 w/v% methylcellulose solution and administered to the animals daily by oral gavage in a volume of 0.1 mL/10 g body weight, using an animal-feeding needle. The anti-EGFR antibody, cetuximab (1 mg/injection) or placebo (PBS) was injected intraperitoneally twice a week to assess the effects of combination therapy with efatutazone. Caliper measurements were made twice a week using digital calipers, and the tumor volumes were estimated using the following formula: $V = L \times W \times D \times \pi/6$, where V is the tumor volume, L is the length, W is the width, and D is the depth (30, 34).

Statistical analysis

Comparisons between treatment groups were made using 2-tailed paired or unpaired Student t tests, as appropriate, based on the results of F tests. The Mann–Whitney U test was used in the event of a nonnormal distribution. The log-rank test was used for survival analysis, and the Kaplan–Meier method was used to assess survival time distribution. For analyses of esophageal cancer-specific mortality, deaths as a result of causes other than ESCC were censored. Univariate Cox regression analysis was also performed. The independent effect of PPAR-γ on mortality was assessed by performing multivariate Cox regression analysis. Statistical significance was defined as a P value <0.05. All data were processed and analyzed using the PASW Statistics 18 software program.

Study approval

All animal procedures and care were approved by the Animal Care and Use Committee of Kumamoto University (approval number H24347). Written informed consent was obtained from the human subjects.

Results

PPAR-γ expression in the normal epithelium and ESCC

We investigated PPAR-γ expression in normal esophageal epithelial samples and tumor lesions from 145 patients with resectable ESCC using immunohistochemical analysis (Supplementary Table S1). PPAR-γ was ubiquitously expressed in the squamous layer of the normal esophageal epithelium in all 145 patients, and there was no variation (Fig. 1A). The positive staining of PPAR-γ was detected in 36 (24.8%) tumors in the patients with ESCC. PPAR-γ expression exhibited a significant inverse relationship with Ki-67 expression ($P < 0.001$, Mann–Whitney U test; Fig. 1B–D).

A recent study reported on the relationship between PPAR-γ expression and prognosis in colorectal cancer (35), and PPAR-γ mRNA expression has demonstrated prognostic value in ESCC

Published OnlineFirst November 22, 2013; DOI: 10.1158/0008-5472.CAN-13-1836

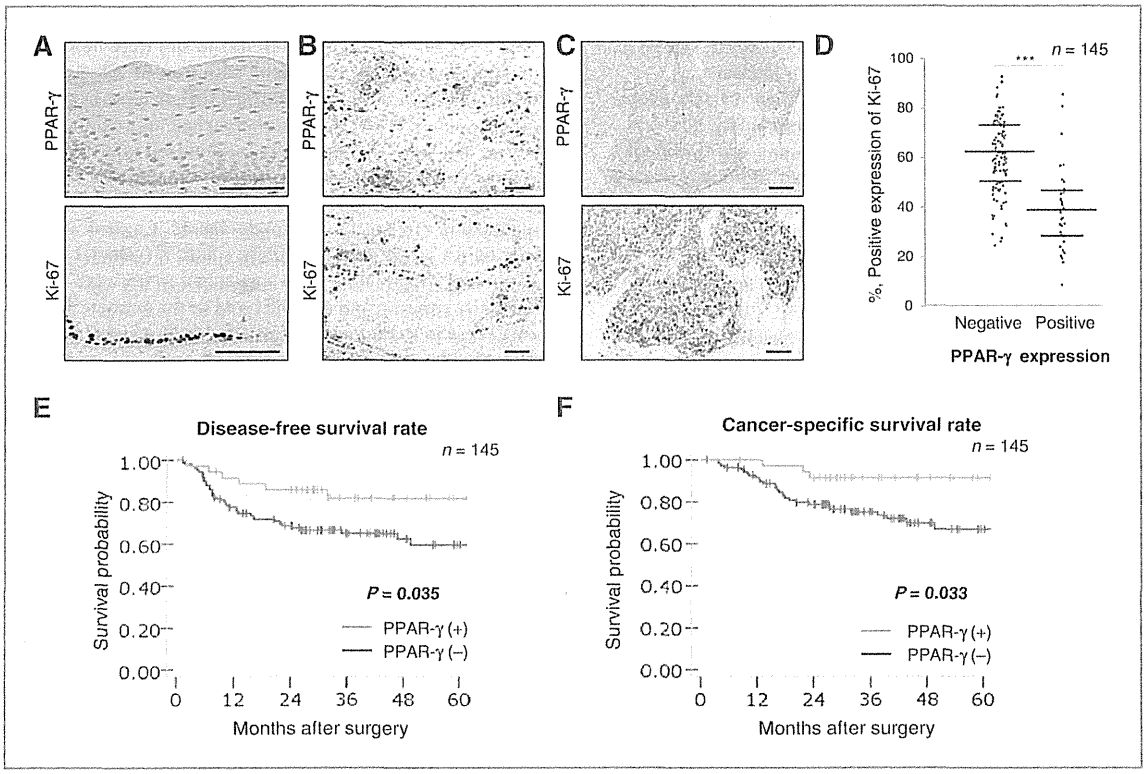

Figure 1. Expression of PPAR-γ and Ki-67 in tissue samples from 145 patients with ESCC. A, immunohistochemistry of PPAR-γ and Ki-67 in normal esophageal squamous epithelium. B, PPAR-γ–positive and Ki-67 negative in an ESCC specimen. C, PPAR-γ–negative and Ki-67 positive in an ESCC specimen. Scale bar, 50 μm. D, relationship between the expression levels of PPAR-γ and Ki-67 ($n = 145$). The horizontal bars show median 25th and 75th percentiles. E and F, Kaplan–Meier curves according to PPAR-γ status. ***, $P < 0.001$ (Mann–Whitney U test).

($n = 55$; ref. 31). However, the relation between PPAR-γ protein expression and prognosis in ESCC remains unclear. According to this study, PPAR-γ expression was associated with a good prognosis in terms of disease-free survival (log-rank $P = 0.035$; Fig. 1E) and esophageal cancer-specific survival (log-rank $P = 0.033$; Fig. 1F) in the 145 patients with ESCC according to univariate and multivariate Cox regression analysis (Supplementary Table S2).

We therefore hypothesized that PPAR-γ was associated with tumor-suppressive effects against ESCC, and that efatutazone, a novel third-generation PPAR-γ agonist, could be a potentially useful anticancer agent in patients with ESCC.

PPAR-γ expression in ESCC cell lines and antiproliferative effects of efatutazone

PPAR-γ expression was examined in 9 human ESCC cell lines and in the colon cancer cell line HT-29, which was used as a positive control for PPAR-γ expression (36). Various levels of PPAR-γ expression were observed in the ESCC cell lines (Fig. 2A). However, efatutazone demonstrated antiproliferative effects in all 9 ESCC cell lines (Fig. 2B). We investigated antiproliferating effects and underlying mechanism of efatutazone using TE-4, TE-8, and TE-11, TE-6 cells, which express high, medium and low levels of PPAR-γ, respectively.

We used 3 siRNAs for PPARG to confirm that the antitumor effects of efatutazone occurred in a PPAR-γ–dependent manner. We selected TE-8 cells, because the PPAR-γ expression of TE-8 cells was strongly suppressed at both the mRNA and protein levels using siRNAs for PPARG (Fig. 2C and D; Supplementary Fig. S2A and S2B). TE-8 ESCC cells were transfected with PPARG siRNA for 48 hours, followed by treatment with control (DMSO) or 50 μmol/L efatutazone for 48 hours. In the presence of the scrambled siRNA (negative control), efatutazone enhanced the expression of pyruvate dehydrogenase kinase isozyme-4 (PDK4), which is an established marker for the activity of PPAR-γ as a transcriptional factor (37, 38), by 2.5-fold compared with the control level, but this effect was blocked in the presence of PPARG siRNA (Fig. 2E). The inhibition of proliferation by efatutazone was related to the PDK4 mRNA level (Fig. 2F). Efatutazone inhibited the proliferation of the ESCC cell lines in a time-dependent manner (Fig. 2G), and PDK4 levels were also increased in a similarly time-dependent manner and correlated with antiproliferative effect of efatutazone (Fig. 2H). The mRNA level of PDK4 after treatment with 25 μmol/L efatutazone was increased more than after treatment with 25 μmol/L troglitazone (Supplementary Fig. S3A). No significant antiproliferative effects of treatment with troglitazone were detected compared with the

Published OnlineFirst November 22, 2013; DOI: 10.1158/0008-5472.CAN-13-1836

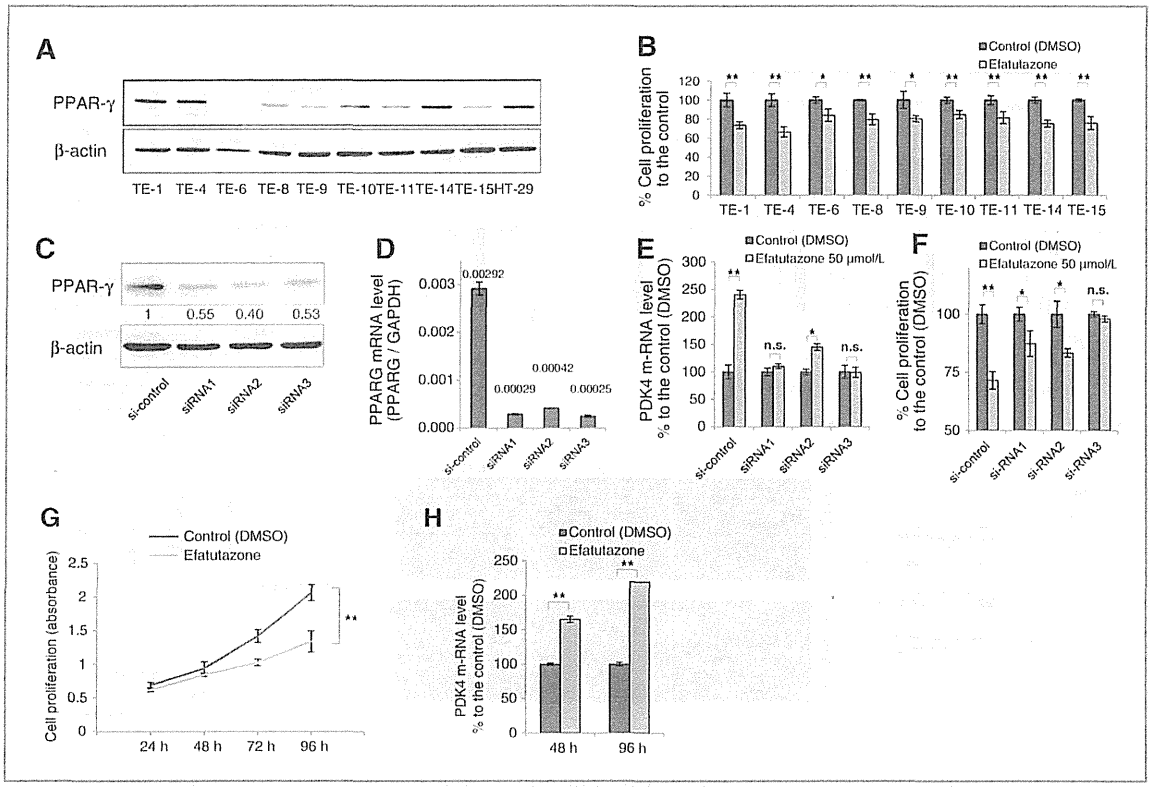

Figure 2. PPAR-γ expression in ESCC lines and *in vitro* antiproliferative effects of efatutazone. A, Western blot analysis for PPAR-γ. B, cell proliferation assay in ESCC cell lines treated with 25 μmol/L efatutazone for 3 days. C, Western blot analysis for PPAR-γ in TE-8 cells after transfection with a scrambled siRNA or 3 kinds of siRNA for PPARG. D, PPARG mRNA levels in TE-8 cells were examined by real-time RT-PCR. E, PDK4 mRNA levels in TE-8 cells after treatment with 50 μmol/L efatutazone for 48 hours were compared with control (DMSO) cells. F, proliferation of TE-8 cells after treatment with 50 μmol/L efatutazone for 48 hours was compared with that of control (DMSO) cells. G, cell proliferation assay in TE-4 cells treated with 25 μmol/L efatutazone. H. PDK4 mRNA levels in TE4 cells after treatment with 25 μmol/L efatutazone were compared with those of control cells. n.s., not significant; *, $P < 0.05$; **, $P < 0.01$ (Student *t* test).

control, however, the proliferation of both TE-4 and TE-8 cells was inhibited by the treatment with efatutazone (Supplementary Fig. S3B). Because the antiproliferative effects of efatutazone were observed in various ESCC cell lines, we investigated the mechanism underlying the antiproliferative effects of efatutazone using TE-4 cells, which highly express PPAR-γ.

In vitro antiproliferative effects of efatutazone in ESCC cells and dependence on Akt-p21Cip1

Efatutazone was previously reported to inhibit cell cycle progression via p21Cip1 in anaplastic thyroid carcinoma (4, 5). In order to clarify the effects of efatutazone on the cell cycle in ESCC, we subjected TE-4 and TE-11 cells to cell cycle analysis by flow cytometry. Accumulation of cells in the G_1 phase, and reductions in the S and G_2/M phases occurred after treatment with efatutazone for 48 hours (Fig. 3A, Supplementary Fig. S4A). In addition, PDK4 mRNA levels were upregulated by treatment with efatutazone for 48 hours, whereas p21Cip1 mRNA levels remained unaffected by the treatment (Fig. 3). However, p21Cip1 protein levels were significantly upregulated in Western blot analysis (Fig. 3C). We therefore focused on the posttranslational modification of the p21 protein (39).

Activation of Akt, which associates with p21Cip1 and phosphorylates it at threonine 145 (Thr145), results in increased cytoplasmic localization of p21Cip1 in breast cancer (40). We therefore stimulated the phosphoinositide 3-kinase (PI3K)–Akt pathway with EGF (100 ng/mL) to investigate these signaling changes in the ESCC cell lines. We found that Akt was activated by treatment with EGF, and p21Cip1 was then gradually phosphorylated at Thr145 in ESCC cells (Fig. 3D).

We treated TE-4 cells with efatutazone for 48 hours, followed by stimulation with or without EGF for 10 minutes to determine if efatutazone was associated with inactivation of Akt. Efatutazone reduced the phosphorylation of both Akt at Ser473 and p21 at Thr145 (Fig. 3E). Localization of p21Cip1 was confirmed by confocal microscopy. Some p21Cip1 protein was detected in the cytoplasm in control cells, but strong staining was detected in the nucleus following treatment with efatutazone for 48 hours (Fig. 3F).

The PPAR-γ expression of TE-6 cells was lower (Fig. 2A) and the antiproliferative effects of treatment with efatutazone were

Published OnlineFirst November 22, 2013; DOI: 10.1158/0008-5472.CAN-13-1836

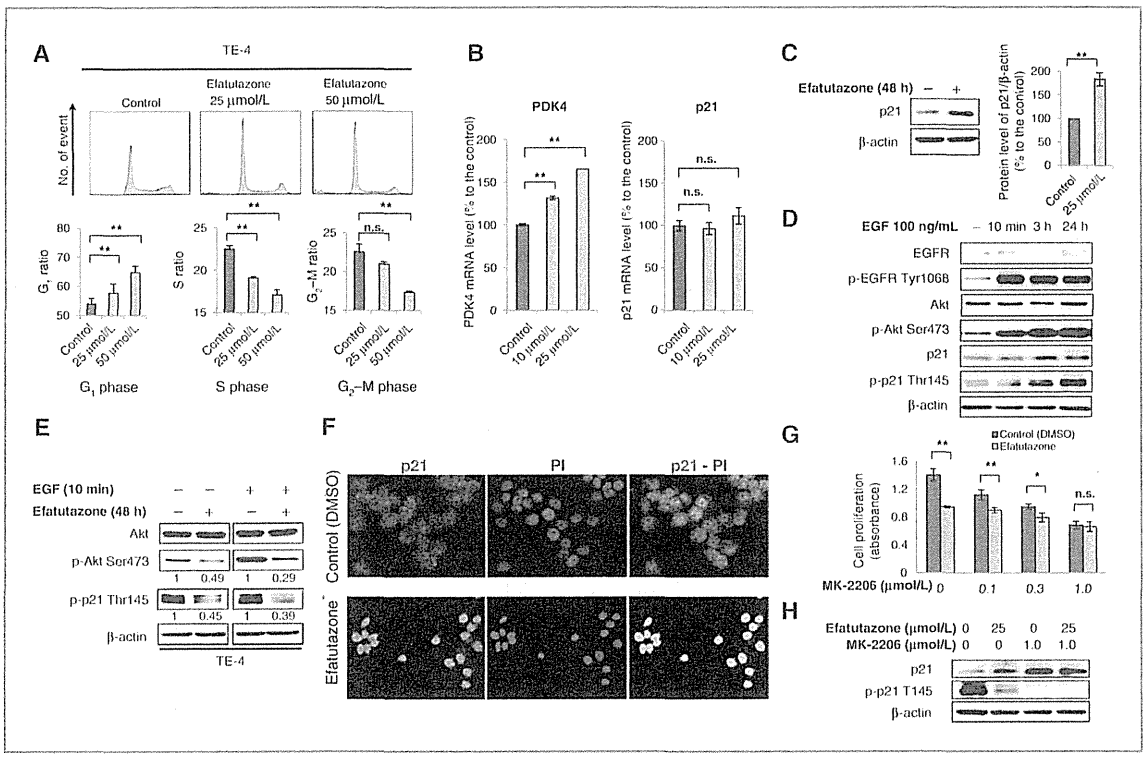

Figure 3. Antiproliferative effects of efatutazone in ESCC cells occur via p-Akt-p21Cip1. A, cell cycle analysis in TE-4 cells after treatment with efatutazone for 48 hours. B, PDK4 and p21Cip1 mRNA levels after treatment with efatutazone for 48 hours. C, Western blot analysis for p21 in TE-4 cells treated with 25 μM efatutazone for 48 hours. Whole cell lysates were examined in three independent experiments and the average and standard division of the p21 protein level was calculated. D, Western blot analysis for EGFR (p-EGFR), Akt (p-Akt), and p21 (p-p21) in TE-4 cells treated with EGF (100 ng/mL) for various times. E, TE-4 cells treated with 25 μmol/L efatutazone, followed by stimulation with or without EGF (100 ng/mL). Whole cell lysates were analyzed by Western blot analysis. F, localization of p21Cip1 after treatment with 25 μmol/L efatutazone for 48 hours was examined by confocal microscopy. Original magnification, ×600. G, antiproliferative effects of efatutazone or control, in combination with various concentrations of MK-2206 for 72 hours, assessed in TE-4 cells. H, Western blot analysis for p21 (p-p21) in TE-4 cells treated with control, efatutazone alone, MK-2206, or efatutazone combined with MK-2206 for 48 hours. n.s., not significant; *, $P < 0.05$; **, $P < 0.01$ (Student t test).

lower than those observed in the other ESCC cell lines (Fig. 2B). We showed that the dephosphorylation of both Akt Ser473 and p21 Thr145 in the TE-6 cells was lower than that observed in TE4 cells (Fig. 3E and Supplementary Fig. S4B). Treatment with efatutazone could not dephosphorylate Akt at Ser473 in TE-8 cells after treatment with siRNA for PPARG (Supplementary Fig. 4C). These data indicated that inactivating the Akt pathway was one of the major targeted effects of efatutazone.

Furthermore we used the Akt inhibitor MK-2206 to detect the association between the antiproliferative effects of efatutazone and inactivation of Akt. The antiproliferative effects of efatutazone compared with the control decreased with increasing dose of MK-2206 (Fig. 3G). The antiproliferative effects were correlated with p21 protein levels and were inversely related to phosphorylation of p21 at Thr145 (Fig. 3H).

These data indicate that efatutazone regulates p21Cip1 protein levels in the nucleus by inactivating Akt and dephosphorylating p21 at Thr145, without affecting the transcription of p21Cip1.

In vivo antiproliferative effects of efatutazone

To the best of our knowledge, no previous studies have demonstrated the antiproliferative effects of conventional PPAR-γ agonists, such as troglitazone, against ESCC cell lines *in vivo*. We therefore compared 3 treatments in a mouse xenograft model established using TE-4 ESCC cells. Animals were divided into a control group, a troglitazone group and an efatutazone group. Tumor volume did not differ significantly between the control group and the troglitazone group; however, a 49.6% ± 13.6% (average ± SD) reduction in tumor volume was observed in the efatutazone group compared with the control group (Fig. 4A, Supplementary Fig. S5A). The mRNA expression of PLIN2, one of the markers for the activity of PPAR-γ as a transcriptional factor, was doubled in the efatutazone group compared with the control group. The mRNA expression levels of p21Cip1 and p27 were not increased by efatutazone treatment (Fig. 4B, Supplementary Fig. S5B), but p21Cip1 protein levels were significantly upregulated (Fig. 4C).

We therefore investigated the phosphorylation status of Akt at Ser473 and of p21 at Thr145. Inactivation of Akt and

Published OnlineFirst November 22, 2013; DOI: 10.1158/0008-5472.CAN-13-1836

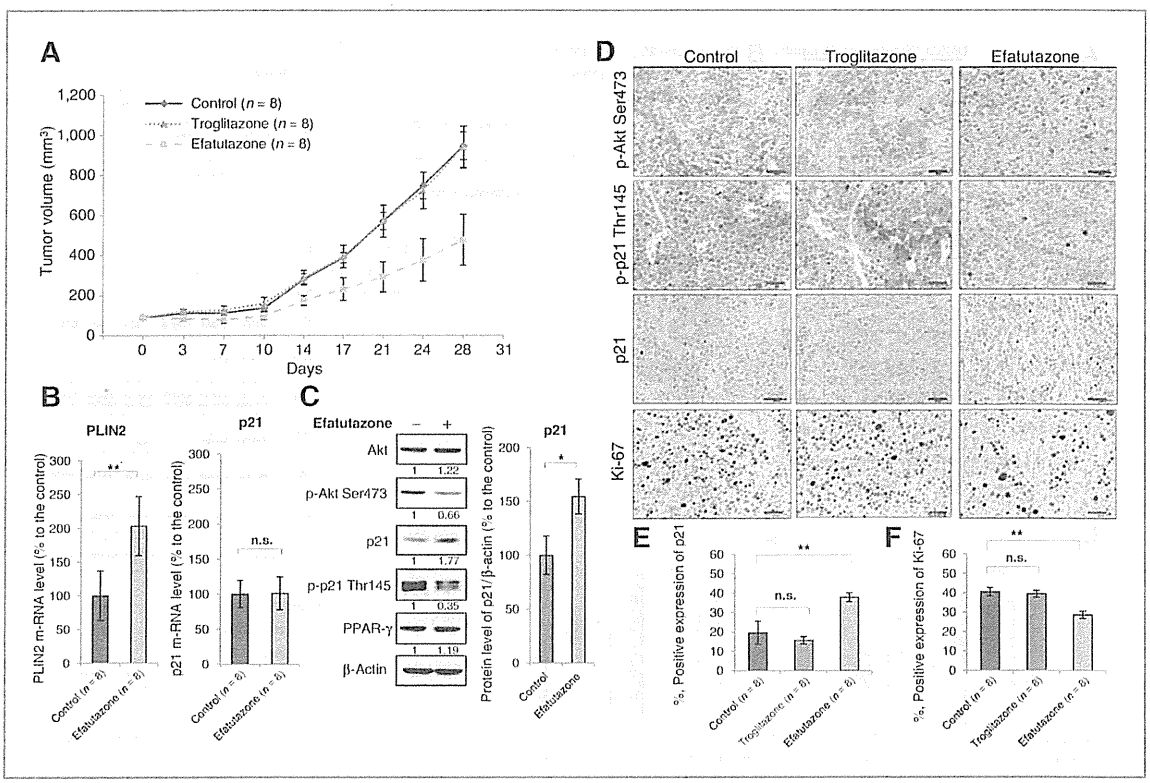

Figure 4. Antitumor effects of efatutazone in human tumor xenograft models. A, growth of TE-4 xenografts treated with control, troglitazone, or efatutazone daily. B, mRNA expression levels of PLIN2 and p21Cip1 in TE-4 cells. C, Western blot analysis for Akt (p-Akt), p21 (p-p21), and PPAR-γ in TE-4 xenografts. The p21 protein level was examined in three independent TE-4 xenografts and the average and standard division of the p21 protein level was calculated. D, immunohistochemical analysis for p-AKT, p-p21, p21, and Ki-67 in TE-4 xenografts. Scale bar, 50 μm. E and F, the rate of positive staining for p21 and Ki-67 in the nucleus of TE-4 xenografts. n.s., not significant; **, $P < 0.01$ (Student t test).

dephosphorylation of p21 at Thr145 were detected more frequently in the efatutazone group than the control group (Fig. 4C). Immunohistochemical staining also demonstrated dephosphorylation of Akt at Ser473 and p21 at Thr145 in the cytoplasm in the efatutazone group (Fig. 4D). We immunohistochemically examined the expression levels of both p21Cip1 and Ki-67 in the nucleus and found that the rate of positive staining for p21Cip1 was significantly increased (Fig. 4D and E), whereas that for Ki-67 was significantly decreased (Fig. 4D and F) by efatutazone compared with both the control and troglitazone groups.

Efatutazone activates EGFR/MAPK signaling

The antiproliferative effects of efatutazone were associated with dephosphorylation of Akt at Ser473. Because Akt is downstream of EGFR signaling via the PI3K–Akt pathway, we investigated the phosphorylation of EGFR at tyrosine 1068 (Tyr1068). We confirmed that efatutazone inactivated Akt pathway within 3 hours, whereas efatutazone gradually phosphorylated EGFR at Tyr1068 for 24 hours in TE-4 cells *in vitro* (Fig. 5A). Furthermore, using conditioned medium (Supplementary Fig. S6), we found that phosphorylation of EGFR was not caused by efatutazone directly, but was induced by medium from efatutazone-treated in TE-4 cells (Fig. 5B). These data indicated that secreted factors after treatment with efatutazone stimulated phosphorylation of EGFR at Tyr1068 in ESCC cells. We confirmed that activated EGFR was detected in 3 ESCC cell lines, TE-4, TE-8, and TE-11 cells after treatment with efatutazone for 48 hours *in vitro* (Fig. 5C). Tyr1068 of EGFR was significantly phosphorylated following treatment with efatutazone, and extracellular signal–regulated kinase (ERK) 1/2 was phosphorylated at Thr202/Tyr204 in TE-4 xenograft tumor lysates, compared with both control and troglitazone-treated tumors (Supplementary Fig. S7A and S7B). EGFR phosphorylation at Tyr1068 and ERK 1/2 phosphorylation at Thr202/Tyr204 were also detected in xenograft tumor lysates from all 3 cell lines (Fig. 5D). Immunohistochemical staining showed activated EGFR at the membrane in TE-4 xenografts after treatment with efatutazone (Fig. 5E).

In vitro effects of combination of efatutazone and MEK inhibitor or anti-EGFR antibody

Importantly, the antiproliferative effects of efatutazone were associated with inactivation of Akt, whereas EGFR/MAPK (mitogen-activated protein kinase) signaling was activated.

Published OnlineFirst November 22, 2013; DOI: 10.1158/0008-5472.CAN-13-1836

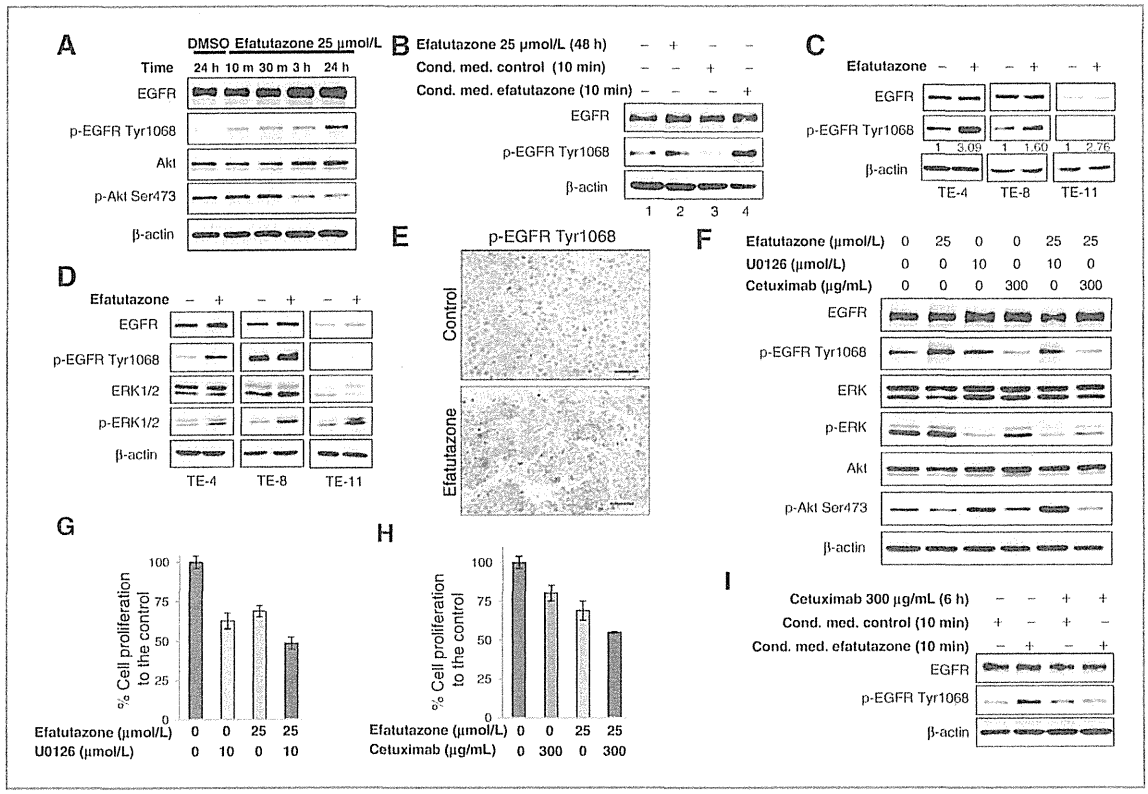

Figure 5. Treatment with efatutazone led to phosphorylation of EGFR and activation of MAPK pathway. A, Western blot analysis for EGFR (p-EGFR) and Akt (p-Akt) in TE-4 cells for various times after treatment with efatutazone. B, TE-4 cells were treated with control (lane 1) or efatutazone (lane 2) for 48 hours, and the medium was collected. Conditioned medium (cond. med.) control and cond. med. efatutazone were adjusted to have the same density of both efatutazone and DMSO. TE-4 cells were treated with these conditioned media (lanes 3, 4) for 10 minutes, and EGFR (p-EGFR) was then determined. C, Western blot analysis for EGFR (p-EGFR) after treatment with 25 μmol/L efatutazone for 48 hours *in vitro*. D, Western blot analysis for EGFR (p-EGFR) and ERK (p-ERK) using whole cell lysates of xenografts. E, immunohistochemical analysis of p-EGFR in TE-4 xenografts. Scale bar, 50 μm. F, Western blot analysis for EGFR (p-EGFR), ERK (p-ERK), and Akt (p-Akt) in TE-4 cells treated for 24 hours. G, percentage of inhibiting effect of TE-4 cells after treatment with U0126, efatutazone, and efatutazone combined with U0126 compared with control. H, percentage of inhibiting effect of TE-4 cells after treatment with cetuximab, efatutazone, and efatutazone combined with cetuximab compared with control. Representative experiments, $n = 3$, mean ± SE. I, TE-4 cells were pretreated with or without cetuximab (300 μg/mL) for 6 hours, followed by stimulation with the conditioned media.

We therefore used molecular-targeted agents in combination with efatutazone to suppress MAPK or EGFR signaling.

The MEK inhibitor U0126 (Supplementary Fig. S8A) was used in combination with efatutazone. Dephosphorylation of ERK 1/2 was detected after treatment with efatutazone combined with U0126. However, EGFR/Akt signaling was activated by combined treatment, compared with treatment with efatutazone alone (Fig. 5F). The growth inhibitory effects of U0126, efatutazone, and the combination of the 2 agents were 37.3 ± 5.0, 31.1 ± 3.6, and 51.6 ± 3.9, respectively, compared with the control (Fig. 5G, Supplementary Fig. S8B).

The anti-EGFR antibody cetuximab (Supplementary Fig. S8C and S8D) was also investigated in combination with efatutazone. Significantly, phosphorylation of EGFR at Tyr1068 caused by treatment with efatutazone was not detected after treatment with the combination of efatutazone and cetuximab. Furthermore, both the PI3K–Akt and MAPK pathways were inactivated by this combination therapy (Fig. 5F). The growth inhibitory effects of cetuximab, efatutazone, and efatutazone combined with cetuximab were 19.7 ± 6.1, 31.1 ± 3.6, and 44.9 ± 0.5, respectively, compared with the control (Fig. 5H, Supplementary Fig. S8E). Interestingly, treatment with efatutazone-conditioned medium for 10 minutes activated EGFR, however EGFR was not phosphorylated at Tyr1068 when TE-4 cells were pretreated with cetuximab for 6 hours (Fig. 5I).

In vivo effects of combination therapy with efatutazone and cetuximab

Cetuximab exhibited better efficacy than U0126 when used in combination with efatutazone *in vitro*. We therefore investigated the antiproliferative effects of efatutazone combined with cetuximab in a mouse TE-4 cell xenograft model. Mice were divided into 4 treatment groups: control group, efatutazone group, cetuximab group, and combination group (Fig. 6A). The tumor inhibitory effects after treatments were

Published OnlineFirst November 22, 2013; DOI: 10.1158/0008-5472.CAN-13-1836

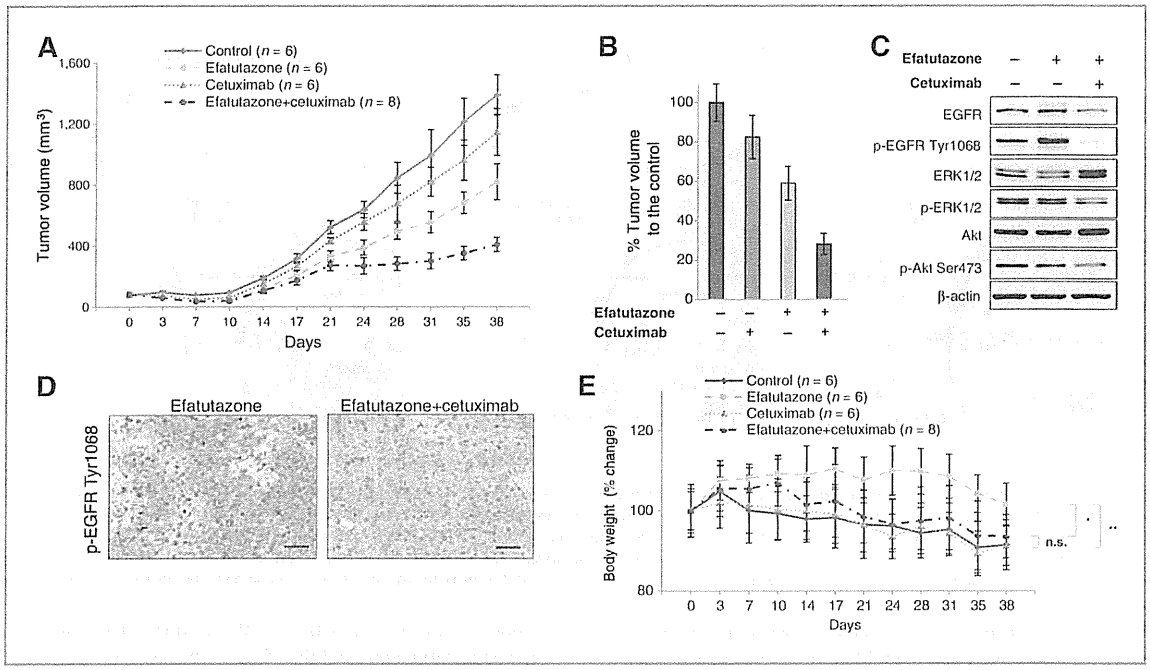

Figure 6. *In vivo* effects of combination therapy using efatutazone with cetuximab. A, growth of TE-4 tumors implanted in nude mice. B, percentage of inhibiting effect after treatment with cetuximab, efatutazone alone, or efatutazone combined with cetuximab compared with control. C, Western blot analysis for EGFR (p-EGFR), ERK (p-ERK), and Akt (p-Akt) in TE-4 cells after treatment. D, immunohistochemical analysis of p-EGFR in TE-4 xenografts after treatment. Scale bar, 50 μm. E, body weights of mice. n.s., not significant; *, $P < 0.05$; **, $P < 0.01$ (Student *t* test).

17.6% ± 11.0%, 41.0% ± 8.5%, and 71.7% ± 5.4% (average ± SD) in the cetuximab group, efatutazone group, and combination group, respectively, compared with the control group after 38 days (Fig. 6B).

EGFR was more dephosphorylated in the combination-treatment group than in the control group, and inactivation of both the PI3K–Akt and MAPK pathways was demonstrated (Fig. 6C). Activation of EGFR at the membrane in TE-4 xenografts after treatment with efatutazone was suppressed in tumors of animals treated with efatutazone plus cetuximab, as demonstrated by immunohistochemical staining (Fig. 6D).

The body weights of the mice were measured twice a week. The mice treated with efatutazone alone tended to gain more weight than control mice, but the body weights of mice treated with efatutazone combined with cetuximab showed no significant difference from the controls (Fig. 6E).

Discussion

PPAR-γ expression is tissue and cancer specific, and the expression of PPAR-γ protein in patients with ESCC and the antiproliferative effects and mechanism of action of the new generation PPAR-γ agonists in ESCC remain unclear. We therefore investigated the expression of PPAR-γ in 145 patients with ESCC, and clearly demonstrated the antiproliferative effects and mechanism of action of the novel PPAR agonist, efatutazone.

We demonstrated that PPAR-γ was expressed in normal esophageal squamous epithelium, and was expressed heterogeneously in ESCC tumors. It exhibited an inverse relationship with Ki-67 expression, as determined by immunohistochemistry.

To the best of our knowledge, efatutazone is the first PPAR-γ agonist shown to inhibit the proliferation of ESCC cell lines both *in vitro* and *in vivo*. Importantly, the results of this study suggest that the novel antiproliferative mechanism of efatutazone involves regulation of p21Cip1 protein levels in the nucleus by inactivating Akt signaling and dephosphorylating p21 at Thr145, without affecting the transcriptional activity of p21Cip1.

The EGFR/MAPK pathway was activated by efatutazone, and combined treatment with efatutazone and cetuximab suppressed both the PI3K–Akt and MAPK pathways, leading to synergistic antiproliferative effects (Fig. 7).

PPAR-γ is affected by endogenous ligands such as $\Delta^{12,15}$ prostaglandin J2, and serves as a transcriptional factor *in vivo* (14). However, the current investigation demonstrated that PPAR-γ expression seems to be heterogeneous during carcinogenesis. In addition, PPAR-γ expression had an inverse relationship with Ki-67 expression, and may be associated with tumor-suppressive effects. We therefore investigated if activation of PPAR-γ by a high-affinity PPAR-γ ligand induced antitumor effects in ESCC.

The conventional PPAR-γ agonist troglitazone partially inhibited ESCC proliferation *in vitro* in previous studies (41). However, our results showed no significant antiproliferative

Published OnlineFirst November 22, 2013; DOI: 10.1158/0008-5472.CAN-13-1836

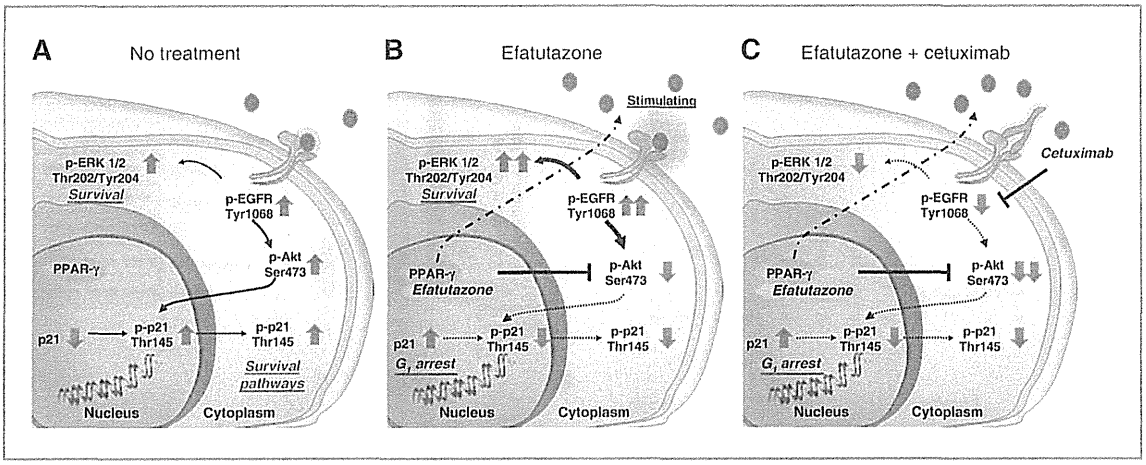

Figure 7. Effects of treatment with efatutazone alone and in combination with cetuximab. A, no treatment. EGFR is phosphorylated by EGF stimulation, and both the PI3K–Akt and MAPK pathways are activated. Activated Akt phosphorylates p21 Thr145 and leads to p21Cip1 translocation from the nucleus to the cytoplasm. Cytoplasmic localization of p21Cip1 is associated with survival pathways. B, efatutazone inactivates Akt, and p21 Thr145 is dephosphorylated. This leads to an increase in the p21Cip1 protein level in the nucleus and G_1 arrest. However, the EGFR/MAPK pathways are activated. C, the combination of efatutazone with cetuximab suppresses both the PI3K–Akt and MAPK pathways and leads to synergistic antiproliferative effects.

effect of troglitazone in ESCC cell lines, whereas efatutazone caused a 49.6% reduction in proliferation of xenografted ESCC cells, and the tumor-reduction rate was similar to the maximum effect of efatutazone against HT-29 colon cancer cells in a previous xenograft study (24). This result suggests that efatutazone represents a promising antitumor agent for patients with ESCC. However, the mechanisms underlying the antiproliferative effects of efatutazone are poorly understood.

This study demonstrated that efatutazone upregulated p21Cip1 protein levels in the nucleus without affecting p21Cip1 mRNA. A previous study showed that Akt activation was associated with phosphorylation of p21 at Thr145, which led to p21Cip1 translocation from the nucleus to the cytoplasm (40). Cytoplasmic p21Cip1 has also been associated with survival pathways (42) and a poor prognosis in breast cancer (43). Interestingly, Akt activation by EGF stimulation also led to phosphorylation of p21 at Thr145 in ESCC, whereas Akt inactivation induced by efatutazone led to dephosphorylation of p21 at Thr145, resulting in upregulation of p21Cip1 protein levels in the nucleus in this study.

Significant tumor regression may be typical for treatments combining PPAR-γ agonists with conventional cytotoxic anticancer agents (4, 23, 24). We found that additional antiproliferative effects were detected in ESCC cell lines when efatutazone was used in combination with 5-fluorouracil, cisplatin or docetaxel *in vitro* (data not shown); however, the antiproliferative effects and mechanism of action of efatutazone in combination with molecular-targeted agents are unclear. Importantly, EGFR/MAPK signaling was activated by efatutazone. EGFR was gradually activated after treatment with efatutazone and the cause of the phosphorylation of EGFR Tyr1068 was a secreted protein (factors) produced by the efatutazone-treated cells. Activation of these pathways may limit the antiproliferative effects of efatutazone, and the addition of molecular-targeted agents to efatutazone may help to suppress these growth pathways. We used U0126 in combination with efatutazone, but the additive effect was small. Recent studies reported ERK-dependent negative feedback in several cancers (44, 45). This ERK-dependent negative feedback was lost after treatment with a MEK inhibitor, and the ability of receptor tyrosine kinase ligands to activate growth signaling was markedly enhanced (44, 46). Similar processes may have been responsible for the effects observed when efatutazone was combined with U0126. ERK-dependent negative feedback was lost after treatment with U0126, and the secreted factors produced by the efatutazone-treated cells stimulated EGFR, followed by the remarkable activation of Akt pathway.

The activation of EGFR induced by the secreted factors after treatment with efatutazone was not detected after pretreating ESCC cells with cetuximab. We therefore used cetuximab in combination with efatutazone, and demonstrated a notable synergistic effect based on signal analysis. This combination therapy may have other benefits. Although the tolerability of efatutazone has been demonstrated in a clinical study, more than half of the patients (51.6%) suffered from peripheral edema, which is a recognized adverse effect of efatutazone treatment (22). In our study, mice treated with efatutazone alone also tended to gain more weight than control mice, although this adverse weight gain was reduced in mice treated with efatutazone combined with cetuximab. A recent study showed that PPAR-γ agonists rapidly stimulated sodium-coupled bicarbonate absorption from the renal proximal tubule, followed by plasma volume expansion. The PPAR-γ agonist–induced transport stimulation was dependent on PPAR-γ–Src–EGFR–ERK (47). In our study, inactivation of MAPK pathway by efatutazone combined with cetuximab may have suppressed the sodium-coupled bicarbonate absorption from the renal proximal tubule and led to a reduction in the adverse weight gain caused by treatment with efatutazone alone.